Quasi-2D Hybrid Perovskite Formation Using Benzothieno[3,2-b]Benzothiophene (BTBT) Ammonium Cations: Substantial Cesium Lead(II) Iodide Black Phase Stabilization

Peer-reviewed author version

DENIS, Paul-Henry; Mertens, Martijn; VAN GOMPEL, Wouter; MAUFORT, Arthur; MERTENS, Sigurd; Wei, ZM; VAN LANDEGHEM, Melissa; GIELEN, Sam; RUTTENS, Bart; Deduytsche, D; Detarvernier, C; LUTSEN, Laurence; Grozema, F; VANDEWAL, Koen & VANDERZANDE, Dirk (2022) Quasi-2D Hybrid Perovskite Formation Using Benzothieno[3,2-b]Benzothiophene (BTBT) Ammonium Cations: Substantial Cesium Lead(II) Iodide Black Phase Stabilization. In: Advanced Optical Materials, 10 (18) (Art N° 2200788).

DOI: 10.1002/adom.202200788
Handle: http://hdl.handle.net/1942/39034

Quasi-2D hybrid perovskite formation using benzothieno[3,2-*b*]benzothiophene (BTBT) ammonium cations: substantial cesium lead(II) iodide black phase stabilization

*Paul-Henry Denis, Martijn Mertens, Wouter T.M. Van Gompel, Arthur Maufort, Sigurd Mertens, Zimu Wei, Melissa Van Landeghem, Sam Gielen, Bart Ruttens, Davy Deduytsche, Christophe Detarvernier, Laurence Lutsen, Ferdinand Grozema, Koen Vandewal, Dirk Vanderzande**

Dr. P-H. Denis, Dr. M. Mertens, Dr. W.T.M. Van Gompel, A. Maufort, S. Mertens, Dr. M. Van Landeghem, Dr. S. Gielen, B. Ruttens, Dr. L. Lutsen, Prof. K. Vandewal, Prof. D. Vanderzande
UHasselt – Hasselt University
Institute for Materials Research (IMO)
Agoralaan 1 – Building D, 3590 Diepenbeek, Belgium
E-mail: dirk.vanderzande@uhasselt.be

Dr. P-H. Denis, Dr. M. Mertens, Dr. W.T.M. Van Gompel, A. Maufort, S. Mertens, Dr. M. Van Landeghem, Dr. S. Gielen, B. Ruttens, Dr. L. Lutsen, Prof. K. Vandewal, Prof. D. Vanderzande
IMEC
Associated lab IMOMEC
Wetenschapspark 1, 3590 Diepenbeek, Belgium

Z. Wei, Prof. F. Grozema
Grozema group
TUDelft
Van der Maasweg 9, 2639 HZ Delft, The Netherlands

Dr. D. Deduytsche, Prof. C. Detavernier
CoCooN
Ghent University
Krijgslaan 281/S1, B-9000 Gent, Belgium

Keywords: photodetectors, moisture stability, thermal stability, low-dimensional perovskites, cesium black phase stabilization

3D hybrid perovskites ($APbX_3$) have made a significant impact on the field of optoelectronic materials due to their excellent performance combined with facile solution deposition and up-scalable device fabrication. Nonetheless, these materials suffer from environmental instability. To increase material stability, the organic cation (A) is substituted by the non-volatile cesium cation. However, the desired photoactive cesium lead(II) iodide black phase is metastable in ambient conditions and spontaneously converts into the photo-inactive yellow δ-phase. In this work, the black phase is stabilized by the formation of a quasi-2D perovskite containing a benzothieno[3,2-*b*]benzothiophene (BTBT) large organic ammonium cation. Thermal analysis shows that degradation of the butylammonium (BA)-based quasi-2D perovskite $(BA)_2CsPb_2I_7$ sets in at ~130 °C, while $(BTBT)_2CsPb_2I_7$ is phase-stable until ~230 °C. Additionally, the $(BTBT)_2CsPb_2I_7$ film doesn't show any sign of degradation after exposure to 77% RH in the dark for 152 days, while $(BA)_2CsPb_2I_7$ degrades in a single day. Photoconductor-type detectors based on $(BTBT)_2CsPb_2I_7$ demonstrate an increased external quantum efficiency and a similar specific detectivity compared to the BA-based reference detectors. Our results demonstrate the utility of employing a BTBT cation within the organic layer of quasi-2D perovskites to significantly enhance the stability while maintaining the optoelectronic performance.

1. Introduction

Three-dimensional (3D) hybrid perovskites with the chemical formula ABX_3 (with monovalent small organic cation A, divalent metal B, and halide X) emerged as an attractive light harvester for optoelectronic applications.[1,2] Perovskite solar cells (PSCs), for instance, have known an unprecedented performance improvement over the last decade, reaching a record efficiency of 25.7%.[3] Despite these spectacular performances, the intrinsic environmental instability of 3D hybrid perovskites hampers their commercial application. The moisture sensitivity and thermal instability of the 3D hybrid perovskite $MAPbI_3$[4–6] is partly related to the volatility of the small methylammonium (MA) cation. When substituted by another small organic cation, formamidinium (FA), the resulting perovskite $FAPbI_3$ displays a higher decomposition temperature than its MA-based counterpart, however, still with a pronounced sensitivity towards humidity.[4,7–10]

As a result, the inorganic cesium (Cs^+) cation has been selected as an alternative nonvolatile species to address the stability issues, yielding the all-inorganic $CsPbX_3$ (X = Cl, Br, and I) with excellent thermal stability.[11–13] However, the black $CsPbI_3$ α-phase with a suitable bandgap of 1.73 eV is metastable below 320 °C in ambient conditions, converting spontaneously into a yellow, photo-inactive, non-perovskite δ-phase.[14,15] In addition, β and γ black phase polymorphs have also been encountered besides the α-phase.[16,17] To benefit from the photoactivity of the $CsPbI_3$ black phase in device applications, it is necessary to improve its phase stability. Some recent approaches towards the phase stabilization of the cesium lead(II) iodide α-phase include halogen exchange,[11,18,19] solvent engineering,[20] and the use of a bication component system.[15] While progress has been made, the phase stability of $CsPbI_3$-containing films still needs to be further improved.

The formation of quasi-2D Ruddlesden-Popper hybrid perovskites $(A')_2A_{n-1}B_nX_{3n+1}$ (with a large organic ammonium cation A', small ammonium cation A, divalent metal cation B, and halide X) has proven to be a practical approach to obtain highly durable perovskite materials.[21–24] Their optoelectronic properties can be systematically tuned through applying the corresponding precursor components in the correct stoichiometric ratio, hereby varying the number of consecutive inorganic layers (n) separated by organic layers.[4,22,25,26] In that respect, a similar approach has been followed to stabilize cesium lead(II) iodide.

Liao et al.[27] initially reported the formation of the cesium lead(II) iodide quasi-2D hybrid perovskite $(BA)_2CsPb_2I_7$ through the incorporation of an aliphatic butyl ammonium (BA) cation. This layered $\langle n \rangle = 2$ hybrid perovskite displayed excellent stability under 30% relative humidity (RH) exposure at 25 °C for two months and thermal stress at 85 °C for three days. Soon after, the aromatic phenyl ethyl ammonium (PEA) cation was systematically introduced into γ-$CsPbI_3$ by Jiang et al.[28] to yield a series of quasi-2D hybrid perovskites $(PEA)_2Cs_{n-1}Pb_nI_{3n+1}$ with $\langle n \rangle$ = 1, 3, 5, 10, 40, and 60. The undesirable yellow orthorhombic δ-phase could be considerably suppressed in the quasi-2D perovskites under an ambient atmosphere compared to the 3D counterpart.

In practice, it has been challenging to form phase-pure $\langle n \rangle$ quasi-2D hybrid perovskite thin films. When a particular layered n hybrid perovskite is targeted, usually a broad distribution of various coexistent layer thicknesses n is present within the film.[29,30] Due to this layer thickness distribution, charge carrier transport within quasi-2D hybrid perovskite films tends to be more complex compared to their pure 3D counterpart.[31,32] It is, therefore, favorable to synthesize quasi-2D hybrid perovskite films with enhanced phase purity. In particular, Hadi *et al.*[33] demonstrated the influence of strongly complexing solvents on the phase-purity of quasi-2D $BA_2Cs_{n-1}Pb_nI_{3n+1}$ films. By establishing iodoplumbate/solvent complexes, a retardation of the crystallite nucleation rate was achieved, which yielded improved phase purity, crystallinity, and film morphology.

Although it has been shown that simple aliphatic or aromatic ammonium cations (e.g., BA or PEA) can be applied towards the stabilization of the cesium lead(II) iodide black phase through

dimension engineering, the insertion of more complex organic ammonium cations, potentially bestowing additional optical properties[34–36] and charge carrier dynamics to the hybrid,[37–42] has not been applied for the same purpose. In addition, approaches to increase the phase purity of quasi-2D hybrid perovskite films have been poorly investigated to date.

In this work, we assess the cesium lead(II) iodide black phase stabilization by a polyheterocyclic aromatic benzothieno[3,2-*b*]benzothiophene (BTBT) cation through quasi-2D hybrid perovskite formation and compare its stabilization effect with the state-of-the-art aliphatic butyl ammonium (BA) cation.

Using (*in-situ*) XRD and UV-vis spectroscopy, we find that both the thermal and moisture stability of the $(BTBT)_2CsPb_2I_7$ thin film are vastly superior with respect to the reference $(BA)_2CsPb_2I_7$ thin film. Time-resolved microwave conductivity (TRMC) measurements reveal that the photoconductivity and charge-carrier diffusion lengths for a $(BTBT)_2CsPb_2I_7$ thin film are slightly increased with respect to the $(BA)_2CsPb_2I_7$ thin film. Moreover, $(BTBT)_2CsPb_2I_7$-based photoconductor-type detectors delivered a higher photocurrent, higher external quantum efficiency (EQE) and similar specific detectivity compared to $(BA)_2CsPb_2I_7$-based ones. We attribute the enhanced photocurrent and EQE to the higher crystallinity and bigger crystallite size of the $(BTBT)_2CsPb_2I_7$ thin film with respect to $(BA)_2CsPb_2I_7$. Our work clearly demonstrates the benefit of employing a large polyheterocyclic aromatic ammonium cation in quasi-2D hybrid perovskites for stable and efficient solution processable optoelectronics.

2. Results and discussion

2.1. Optical, structural and morphological properties

The mono-functionalized benzothieno[3,2-*b*]benzothiophene with a propyl ammonium tethering chain (BTBT) was synthesized according to our previously reported procedure (**Figure S1**).[43] The commercially available *n*-butylamine hydroiodide (BAI) was purified by precipitation from methanol in diethyl ether before use. For the quasi-2D hybrid perovskite films $(BA)_2CsPb_2I_7$ and $(BTBT)_2CsPb_2I_7$ (**Figure 1a**), $\langle n \rangle = 2$ will be used to denote the targeted nominal composition based on the stoichiometry of the precursor solution. Contrastingly, *n* will be used to denote a specific quasi-2D hybrid perovskite $(A')_2A_{n-1}B_nX_{3n+1}$ with a number of layers (*n*) present in the targeted $\langle n \rangle = 2$ thin film, as usually a distribution of different layers is present.

Both $(BA)_2CsPb_2I_7$ and $(BTBT)_2CsPb_2I_7$ films were optimized towards optimal crystallinity and phase purity. This requires the use of a different procedure for these two perovskite materials due to the significant differences in the molecular structure of the organic cations. The precursor solution of $(BA)_2CsPb_2I_7$ with a 0.3 M concentration was spin-coated and thermally annealed at 130 °C. It was shown in the literature that by adding a solvent with high complexation strength to the precursor solution, the phase purity of a $(BA)_2CsPb_2I_7$ thin film could be improved.[33] We, therefore, added a small amount of dimethylacetamide (DMAC) to the $(BA)_2CsPb_2I_7$ precursor solution in DMF to inhibit quasi-3D perovskite formation and favor the crystallization towards the targeted layered $n = 2$ hybrid perovskite. To obtain highly crystalline $(BTBT)_2CsPb_2I_7$ thin films, our previously reported thermal/solvent vapor annealing method was employed using DMSO to enhance the mobility of the rigid BTBT molecules during self-assembly.[43] This annealing method cannot be applied for the BA-containing quasi-2D hybrid perovskite due to the dissolution of the respective thin films in the DMSO vapor environment. Peculiarly, a relatively high annealing temperature of 210 °C was required to obtain highly crystalline $(BTBT)_2CsPb_2I_7$ thin films. We suggest that the formation energy of a $(BTBT)_2CsPb_2I_7$ thin film is significantly higher in contrast to that of $(BA)_2CsPb_2I_7$ due to the limited mobility of the bulky BTBT molecules compared to the small and flexible BA molecules.

The resulting absorption and emission spectra of the quasi-2D hybrid perovskite thin films are shown in **Figure 1b-c**.

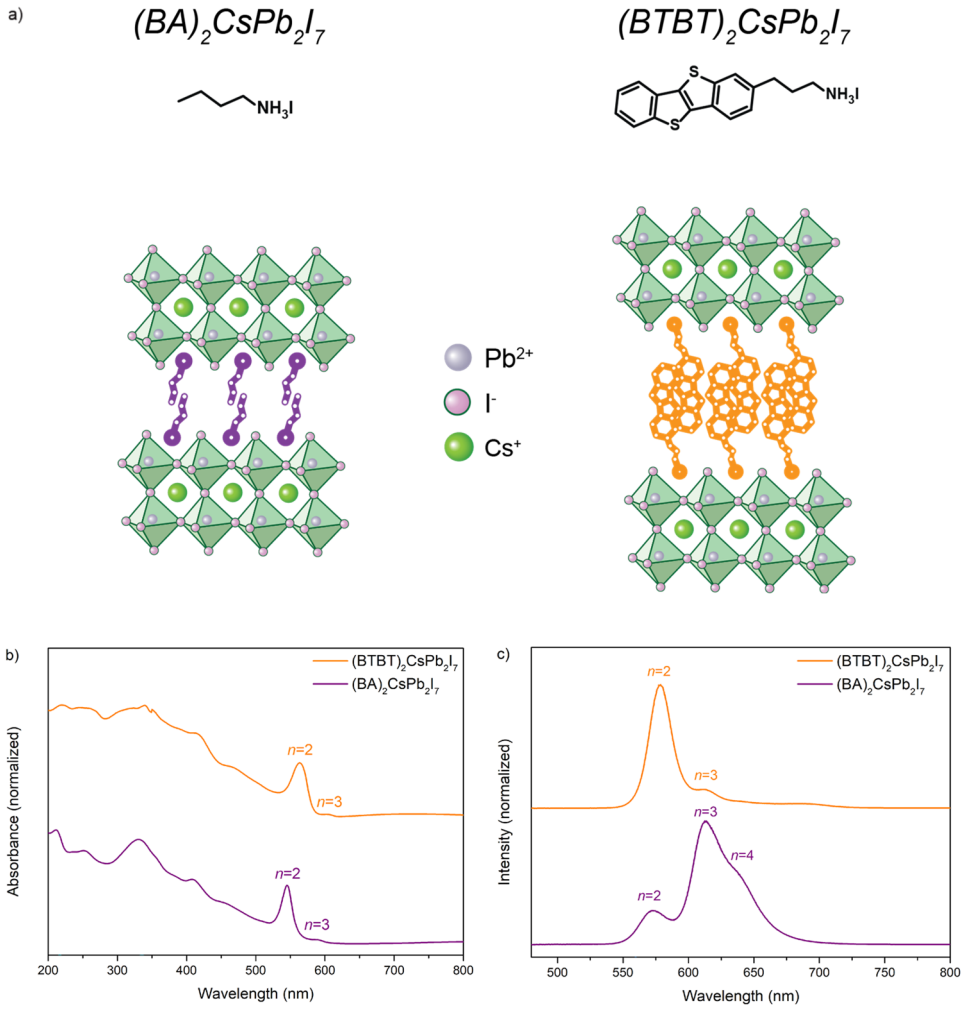

Figure 1. Schematic representation of the quasi-2D hybrid perovskite structures of $(BA)_2CsPb_2I_7$ and $(BTBT)_2CsPb_2I_7$ (a). Absorption (b) and emission spectra (c) of a spin-coated $(BA)_2CsPb_2I_7$ thin film thermally annealed at 130 °C for 10 min, and a $(BTBT)_2CsPb_2I_7$ thin film solvent-annealed at 210 °C for 5 min. The emission spectra were obtained by exciting the samples at 405 nm.

The absorption spectra show that the layered $n = 2$ hybrid perovskites are successfully synthesized based on the appearance of the distinct excitonic absorption peaks at respectively 546 nm for $(BA)_2CsPb_2I_7$,[33] and 565 nm for $(BTBT)_2CsPb_2I_7$ (**Figure 1b**). The optical properties of the previously reported $n = 1$ 2D layered perovskite $(BTBT)_2PbI_4$ were added to the supporting information for comparison (**Figure S4**).[43] The difference in excitonic peak position corresponding to a certain n value is attributed to the nature of the large (BA or BTBT) organic cation, inducing a different degree of distortion of the interconnected corner-sharing lead(II) iodide octahedra.[44] Besides $n = 2$, the excitonic peak corresponding to $n = 3$ is also visible in the absorption spectrum for each sample, though with a much lower intensity relative to $n = 2$.

Photoluminescence (PL) emission spectra reveal additional information concerning the presence of different phases within the thin film samples (**Figure 1c**). As expected, the PL spectra exhibit characteristic excitonic emission peaks that are slightly red-shifted compared to the corresponding absorption peaks. The $(BA)_2CsPb_2I_7$ thin film contains emission peaks corresponding to a distribution of layer thicknesses ($n = 2$, 3, and 4), with emission primarily originating from the layered $n = 3$ hybrid perovskite. For the $(BTBT)_2CsPb_2I_7$ thin film, the

emission originates mainly from the layered n = 2 hybrid perovskite, accompanied by a very weak emission signal of the layered n = 3 hybrid perovskite and quasi-3D cesium lead(II) iodide (650 – 700 nm). We suggest that the appearance of this prominent n = 2 excitonic peak is likely due to the relatively low amount of layered n = 3 perovskite with respect to n = 2 present in the $(BTBT)_2CsPb_2I_7$ film. However, the occurrence of energy funneling toward higher n phases, with the lowest band gap energy, makes a quantitative determination of the ratio between n = 2 and n = 3 phases difficult.[45]

To assess the overall crystallinity of the samples, the XRD patterns of the spin-coated thin films are presented in **Figure 2**.

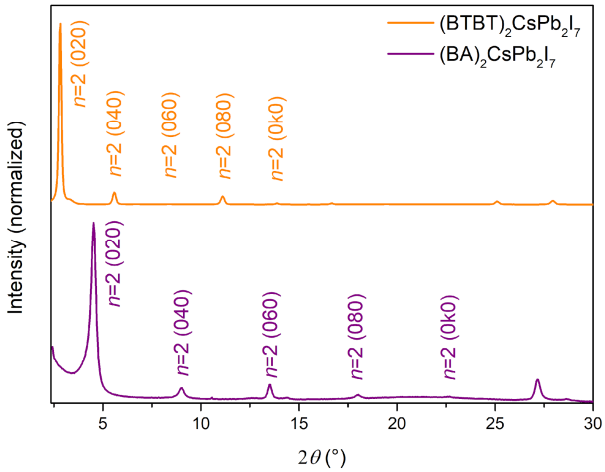

Figure 2. X-ray diffraction pattern of a spin-coated $(BA)_2CsPb_2I_7$ thin film thermally annealed at 130 °C for 10 min, and a $(BTBT)_2CsPb_2I_7$ thin film solvent annealed at 210 °C for 5 min.

The diffraction patterns consist of a series of (0k0) reflections characteristic for a layered n = 2 hybrid perovskite with a preferential growth along the [101] direction, parallel to the substrate surface.[26] The XRD pattern of our $(BA)_2CsPb_2I_7$ film closely matches with those reported in the literature.[32] The interplanar d_{0k0} spacing values of $(BA)_2CsPb_2I_7$, and $(BTBT)_2CsPb_2I_7$ are determined to be 19.6 and 31.6 Å, respectively. With respect to our previously reported n = 1 2D layered perovskite $(BTBT)_2PbI_4$ thin films (**Figure S5**),[43] the d spacing increases by almost 6 Å for n = 2 $(BTBT)_2CsPb_2I_7$. This increase matches exactly with the addition of one lead(II) iodide octahedral sheet to $(BTBT)_2PbI_4$, as expected.[22,47,48]

The crystallite size (D) in both $(BTBT)_2CsPb_2I_7$ and $(BA)_2CsPb_2I_7$ thin films was estimated using Scherrer's equation, based on the FWHM of the first reflection:

$$D = \frac{K\lambda}{\beta cos\theta}$$

with D the crystallite size, K a constant (shape factor, taken here as 1 for crystallites of an unknown shape), λ the wavelength of the X-ray, β the FWHM of the reflection (in radians) and θ the diffraction angle.[49] The crystallite sizes of $(BTBT)_2CsPb_2I_7$ and $(BA)_2CsPb_2I_7$ were calculated to be 57 nm and 12 nm, respectively.

The thin film morphology and roughness of the films were examined by scanning electron microscopy (SEM) and atomic force microscopy (AFM), respectively, and the results are represented in **Figure S6**. The SEM micrographs of $(BA)_2CsPb_2I_7$ and $(BTBT)_2CsPb_2I_7$ reveal full surface coverage with no pinholes. For $(BTBT)_2CsPb_2I_7$, we observe a higher surface roughness based on AFM, in contrast to the smoother $(BA)_2CsPb_2I_7$ thin film. The higher surface roughness of $(BTBT)_2CsPb_2I_7$ compared to $(BA)_2CsPb_2I_7$ can be attributed to the use of the solvent vapor annealing instead of the traditional thermal annealing method, inducing a different microstructure with bigger grains.

2.2. Thermal stability

In-situ temperature-controlled XRD measurements were carried out to study the intrinsic thermal stability of $(BTBT)_2CsPb_2I_7$ and to compare it with the state-of-the-art $(BA)_2CsPb_2I_7$ thin film (**Figure 3**). In this way, we investigate the effect of the addition of a polyheterocyclic aromatic ammonium cation on the cesium lead(II) iodide black phase stabilization with respect to the aliphatic BA one. The samples were heated with incremental steps of 1 °C per min until complete degradation, and XRD patterns were acquired every 10 °C.

From the 2D *in-situ* XRD plot, it is apparent that the $(BA)_2CsPb_2I_7$ thin film is thermally stable until a temperature of approximately 130 °C (**Figure 3a**). Above this temperature, the (0k0) reflections of the layered n = 2 hybrid perovskites start to decrease in intensity due to degradation into lead(II) iodide (inset diffractogram **Figure 3b**: main reflection at ~ 12.6° 2θ).[50] When the aliphatic BA cation is substituted with the BTBT cation, the thermal stability is dramatically enhanced to 230 °C, since no decrease in the intensity of the reflections nor the appearance of reflections corresponding to a degradation phase is apparent below this temperature (**Figure 3c-d**). The *in-situ* XRD patterns with normalized intensities are shown in the SI (**Figure S7**) to be able to investigate the much weaker reflections present at high temperatures that are obscured in the plot with absolute intensities, revealing the degradation of the cesium lead(II) iodide black phase into the yellow δ-phase (reflection at ~ 9.85° 2θ in diffractogram)[28,51] at respectively 180 °C for $(BA)_2CsPb_2I_7$ and 270 °C for $(BTBT)_2CsPb_2I_7$. We suggest that the markedly enhanced stability has its origin in the rigid fused nature of the BTBT cation as compared to the more flexible BA. To study the influence of the organic cation in more detail, a thermal gravimetric analysis (TGA) was performed on powders of the BAI and BTBTI ammonium iodide salts, probing the thermal stability of these large organic ammonium cations exclusively (**Figure S8**). The aliphatic BAI salt shows gradual degradation weight loss under thermal stress starting from RT until approximately 175 °C, whereafter a significant weight loss is observed that may be ascribed to decomposition of the ammonium salt followed by volatilization of butylamine and hydrogen iodide. In contrast, the BTBTI salt reveals no weight loss up to a temperature of almost 260 °C, indicating that the organic ammonium cation remains intact at such high temperatures. We therefore demonstrate that the introduction of a polyheterocyclic aromatic BTBT cation through quasi-2D hybrid perovskite formation effectively stabilizes the cesium lead(II) iodide black phase under thermal stress with respect to an aliphatic one, generating a highly stable active material for optoelectronics.

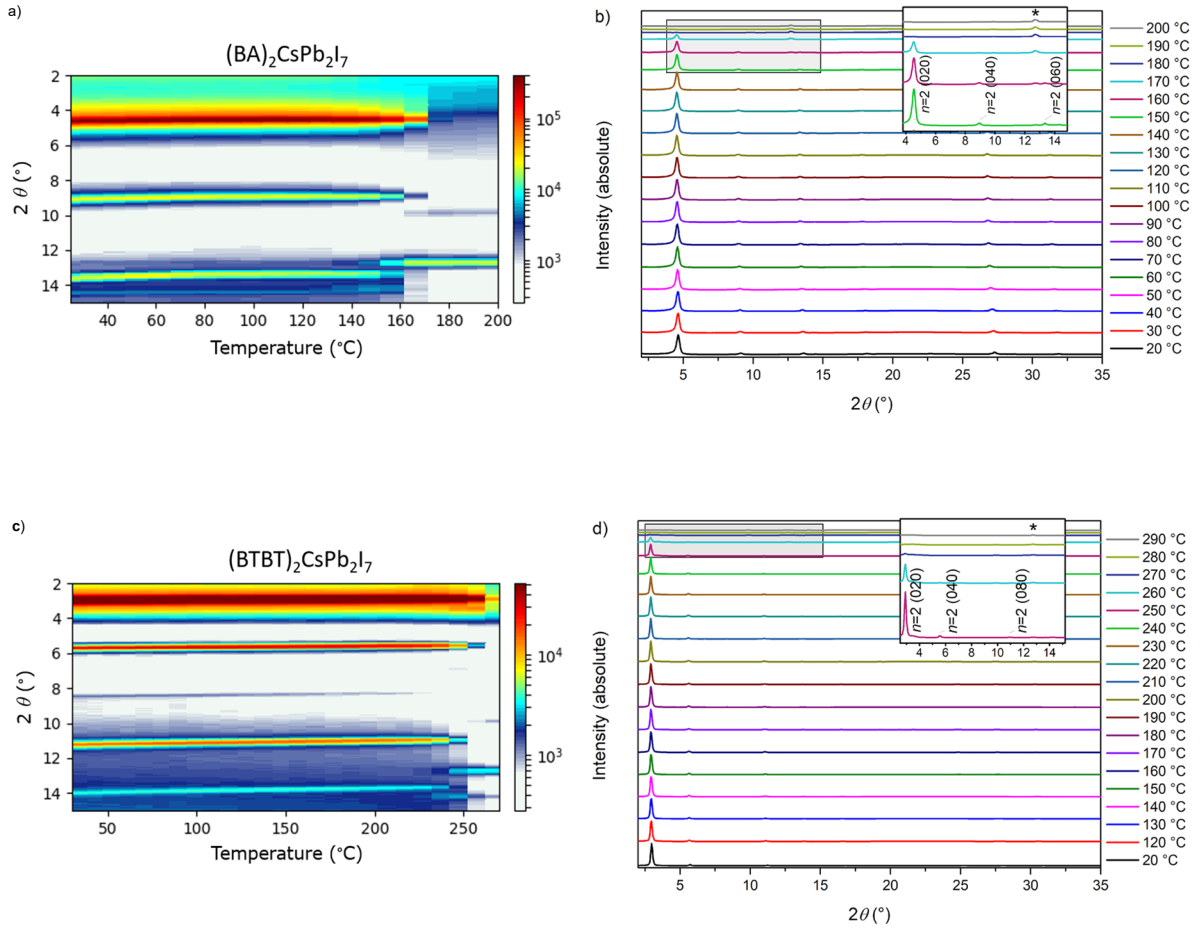

Figure 3. 2D in-situ x-ray diffraction plots as a function of temperature starting from a spin-coated $(BA)_2CsPb_2I_7$ (a), and $(BTBT)_2CsPb_2I_7$ (c) thin film before the in-situ experiment. In-situ X-ray diffraction patterns (absolute intensity) as a function of temperature starting from a spin-coated $(BA)_2CsPb_2I_7$ (b), and $(BTBT)_2CsPb_2I_7$ (d) thin film before the in-situ experiment. The weak reflections of the degradation product PbI_2 (*) are magnified in the respective temperature range.

2.3. Moisture stability

Encouraged by the superior intrinsic thermal stability of the $(BTBT)_2CsPb_2I_7$ thin film (230 °C) as compared to the state-of-the-art reference $(BA)_2CsPb_2I_7$ (130 °C), we decided to study the intrinsic moisture stability of the samples over the course of 152 days under air of 77% relative humidity (RH) in the dark and at room temperature. The UV-vis absorption spectra and normalized XRD patterns of the samples at different times are summarized in **Figure 4**. For the $(BA)_2CsPb_2I_7$ thin film, we observe degradation of the layered $n = 2$ hybrid towards the $n = 1$ 2D layered perovskite $(BA)_2PbI_4$[52] already after one day (excitonic absorption peak at 510 nm, **Figure 4a**; *d* spacing: 13.8 Å, **Figure 4b**). Additionally, degradation into the yellow δ-phase of $CsPbI_3$ (absorption peak around 410-420 nm;[12] reflection at ~ 9.85° 2ϑ in diffractogram), PbI_2 (main reflection at ~ 12.6° 2ϑ in diffractogram) and a potential 1D hybrid phase[53] (with an excitonic absorption peak at 413 nm; *d* spacing: 10.3 Å), occurs. After one month of storage, the $n = 1$ 2D layered perovskite $(BA)_2PbI_4$ and the potential 1D hybrid phase have degraded completely into primarily lead(II) iodide (evinced by the increase of the intensity of the reflection at ~12.6° 2ϑ in the diffractogram) and the yellow δ-phase of $CsPbI_3$.

In contrast, our $(BTBT)_2CsPb_2I_7$ thin film shows excellent resistance against humidity, with no apparent degradation into lead(II) iodide nor a phase transition towards the yellow δ-phase over a period of 152 days, maintaining the excitonic absorption peak at 565 nm (**Figure 4c**) and intense (0k0) reflections in the diffractogram corresponding to a *d* spacing of 31.6 Å that is characteristic for the layered $n = 2$ $(BTBT)_2CsPb_2I_7$ hybrid perovskite (**Figure 4d**). We propose

that the introduction of polyheterocyclic aromatic BTBT molecules increases the hydrophobicity and rigidity of the organic layers compared to the aliphatic BA-containing ones, resulting in enhanced moisture stability and the inhibition of yellow δ-phase formation.[54] The *in-situ* XRD patterns of the moisture stability test with absolute intensities are shown in the ESI for completeness (**Figure S9**).

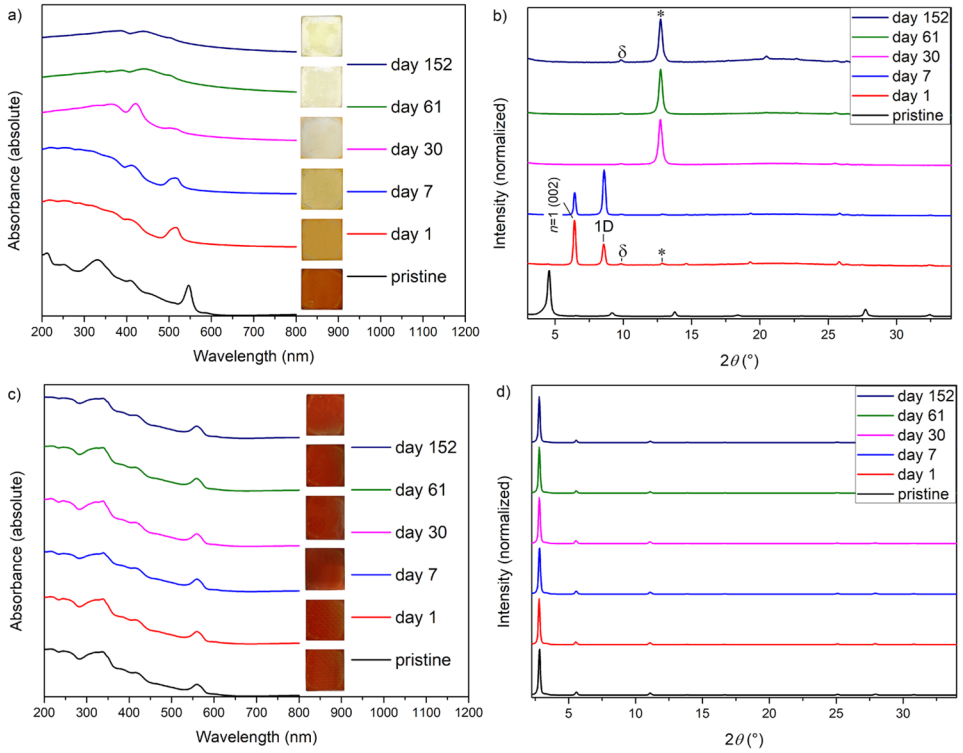

Figure 4. Absorption spectra of a spin-coated $(BA)_2CsPb_2I_7$ thin film that was prepared by annealing at 130 °C for 10 min (a), and of a $(BTBT)_2CsPb_2I_7$ thin film that was prepared by solvent annealing at 210 °C for 5 min (c). Normalized X-ray diffraction patterns of $(BA)_2CsPb_2I_7$ (b) and $(BTBT)_2CsPb_2I_7$ (d) thin films prepared using the same procedure as those used for the absorption spectroscopy measurements. The samples were stored at 77% RH and measured at different times over the course of 152 days. The weak reflections in the XRD patterns belonging to the degradation product PbI_2 (*) and the yellow δ phase (δ) are indicated in the relevant temperature range for $(BA)_2CsPb_2I_7$. For $(BTBT)_2CsPb_2I_7$, these reflections are absent after 152 days of storage.

As indicated by both thermal and moisture stress tests, the incorporation of a BTBT cation clearly significantly enhances the stability of the cesium lead(II) iodide black phase compared to the material system containing aliphatic BA cations.

2.4. Time-resolved microwave conductivity (TRMC)

To investigate the role of the molecular structure of the large organic cation in potentially contributing to the charge transport properties of the hybrid, time-resolved microwave conductivity (TRMC) measurements[22,40,43] were performed on the spin-coated $(BTBT)_2CsPb_2I_7$ and $(BA)_2CsPb_2I_7$ thin films. In TRMC measurements, laser excitation induces mobile charge carriers leading to an increase in the photoconductivity of the thin films, which is measured as a function of time after photo-excitation. The product of the yield and mobility of the charges is related to the maximum photoconductance (ΔG_{max}) by[22]

$$\varphi \Sigma\mu = \frac{\Delta G_{max}}{I_0 \beta e F_A}$$

where φ is the fraction of absorbed photons that leads to mobile charges, $\Sigma\mu = \mu_e + \mu_h$ is the total mobility of charge carriers, I_0 is the number of photons per unit area per pulse, β is the ratio of the inner dimensions of the microwave cell, e is the elementary charge, and F_A is the

fraction of light absorbed by the sample at the excitation wavelength. **Figure 5** shows the time-resolved photoconductivity of the spin-coated $(BTBT)_2CsPb_2I_7$ and $(BA)_2CsPb_2I_7$ thin films.

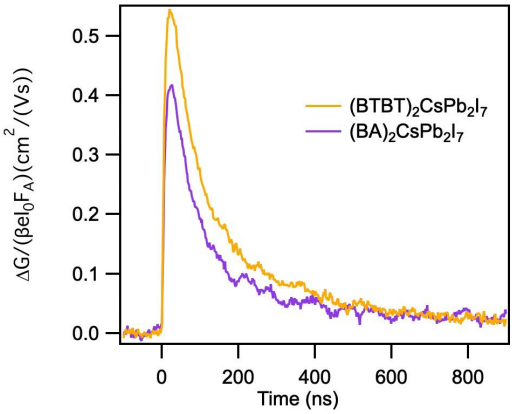

Figure 5. The product of the mobility and yield of charge carriers as a function of time upon photoexcitation with a 500 nm laser pulse with a photon intensity of ~1.8×10^{11} cm^{-2}. This product is directly proportional to that change in conductance on photoexcitation.[55]

Upon excitation, both TRMC traces show a sharp rise due to the generation of free mobile charge carriers. It is evident that the $(BTBT)_2CsPb_2I_7$ thin film shows a higher maximum $\varphi\Sigma\mu$ (0.55 $cm^2V^{-1}s^{-1}$) compared to the reference $(BA)_2CsPb_2I_7$ (0.42 $cm^2V^{-1}s^{-1}$). With the elapse of time, $\varphi\Sigma\mu$ decays due to charge recombination or trapping.[56] Both films show a very similar half-lifetime of the charge carriers of 95 ns and 90 ns for $(BTBT)_2CsPb_2I_7$ and $(BA)_2CsPb_2I_7$ thin films, respectively. Accordingly, we estimated their diffusion lengths of charge carriers ($L_D = \sqrt{D\tau_{1/2}}$ with $D = \frac{\mu k_B T}{e}$ and $\tau_{1/2}$ the half lifetime of the charge carriers) to be ~0.35 µm and ~0.3 µm.

A plausible explanation for the observed similar lifetimes, and slightly higher $\varphi\Sigma\mu$ for the $(BTBT)_2CsPb_2I_7$ thin film is that the incorporation of the BTBT molecules may slightly influence the exciton binding energy, thereby influencing the yield (φ) of dissociation of charges. Furthermore, the locally probed charge carrier mobility by microwaves,[57,58] depends on the crystallinity in the film. Therefore, the larger microwave photoconductivity found in the $(BTBT)_2CsPb_2I_7$ film may also originate from higher film crystallinity. In summary, the polyheterocyclic aromatic BTBT ammonium cation has only a minor influence on the local charge carrier properties compared to the state-of-the-art BA cation. Therefore, we can conclude that using the BTBT cation, a material was obtained with significantly enhanced stability and comparable intrinsic charge transport properties compared to the reference BA cation.

2.4. Optoelectronic device properties

To test the performance of the $(BTBT)_2CsPb_2I_7$ quasi-2D hybrid perovskite with high crystallinity and stability in optoelectronic devices, we fabricated planar photoconductor-type detectors and evaluate their photo-response, external quantum efficiency (*EQE*), and specific detectivity (*D**). The planar architecture was selected since the layered $n = 2$ hybrid perovskites show preferential growth parallel to the substrate surface.[26] The device architecture consists of the respective perovskite film (thickness ~ 200 nm, determined by profilometry) deposited onto a quartz substrate with a 80 nm thickness gold electrode evaporated on top of the thin films. A shadow mask with four interdigitating finger structures was employed to deposit the gold electrode (electrode distances L= 0.05, 0.10, 0.25, and 0.50 mm; corresponding device area A= 0.026, 0.048, 0.080, and 0.120 cm^2; **Figure 6a**). The photocurrent is measured between the different interdigitating electrode fingers by sweeping an applied voltage between -15 V and 15 V over them under a light intensity of 1 sun with a A.M. 1.5 G spectrum (ASTM). The

I-V curves of the photoconductor-type detectors, $(BTBT)_2CsPb_2I_7$ and reference $(BA)_2CsPb_2I_7$, are evaluated under dark and light irradiation and presented in **Figure 6b-c**. Under light irradiation, the $(BA)_2CsPb_2I_7$ detector delivers photocurrents from 4.5 x 10^{-8} to 2 x 10^{-7} A at 15 V by decreasing the electrode distance *L*. This experimental trend is expected as, at the same voltage, the charge carrier transit time ($\tau_t = \frac{L^2}{\mu V}$) shortens, and thus, the amount of charge carrier recombination events are reduced, resulting in an increased EQE for photoconductors..[59] For the detector based on $(BTBT)_2CsPb_2I_7$, we observe a significant increase in light current by one order of magnitude, with photocurrents reaching almost 1.75 x 10^{-6} A at 15 V for the lowest electrode distance under light irradiation. Since only a slightly higher intrinsic photoconductivity was found locally for $(BTBT)_2CsPb_2I_7$ than for $(BA)_2CsPb_2I_7$ by TRMC, we hypothesize that the substantial increase in photocurrent delivered by the $(BTBT)_2CsPb_2I_7$ detector with respect to the BA-containing one, could be attributed to the larger crystallites in the thin film (*vide supra*). While TRMC probes the local (intragrain) charge carrier mobility, the photocurrent in photodetectors is determined by the macroscopic (intergrain) charge carrier mobility. Larger crystallites should lead to a reduced amount of grain boundaries.[60]

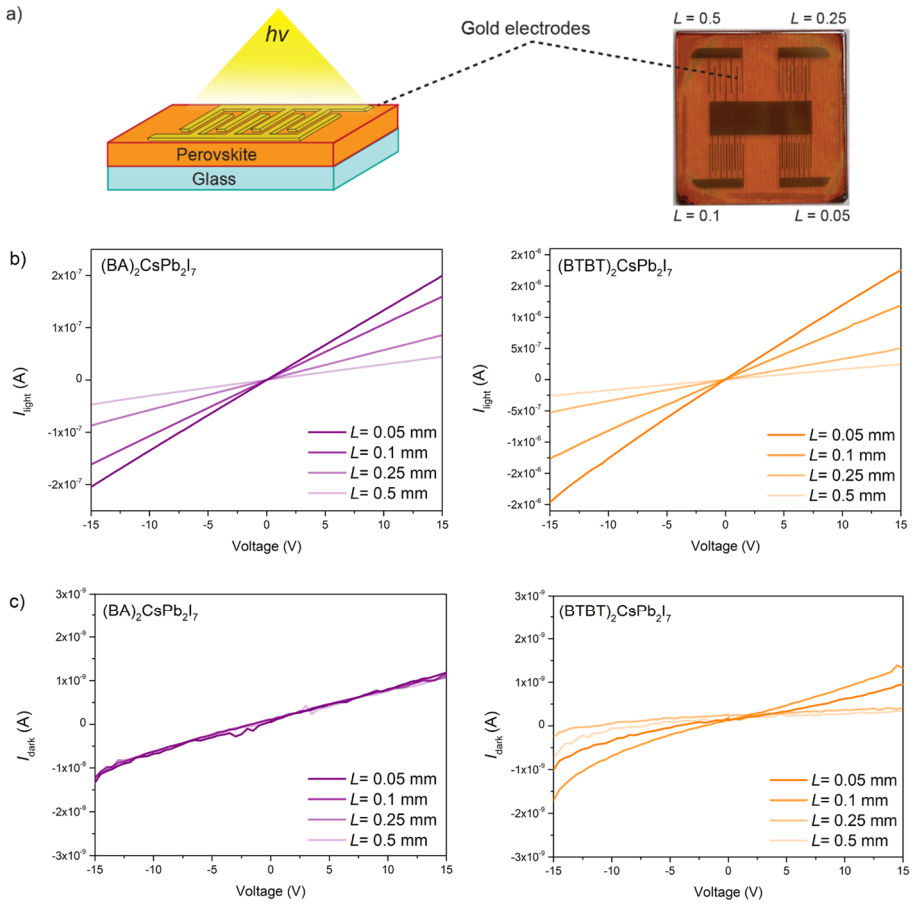

Figure 6. Schematic representation and photograph of the photoconductor-type detector (a). The *I-V* curves of the photoconductor-type detector based on $(BA)_2CsPb_2I_7$, and $(BTBT)_2CsPb_2I_7$, with different electrode distances *L* = 0.05, 0.10, 0.25, and 0.50 mm, under light irradiation (b) and in the dark (c).

The light to dark current ratio (I_{light}/I_{dark}) was estimated for each electrode distance, with $(BTBT)_2CsPb_2I_7$ reaching the highest value of almost 2000 at a voltage bias of 15 V (**Figure S10**). However, as the I_{light}/I_{dark} ratio depends on the amount of light absorbed by the device, a better detector performance metric is given by the specific detectivity *D**.

It is estimated based on the ratio of the responsivity ($R = \frac{EQE*\lambda*e}{hc}$), with EQE the external quantum efficiency, λ the wavelength, e the elementary charge, h the Planck constant, and c speed of light) and the noise current (i_{noise}), assuming a bandwidth (Δf) near 1 Hz:[61,62]

$$D^*(Jones) = \frac{R\sqrt{A\Delta f}}{i_{noise}}$$

The noise current was determined by considering the following noise sources: white shot and thermal noise.[62,63] Flicker noise is neglected, which can be done when the devices operate at a sufficiently high frequency.[64] The white shot noise (i_{shot}) is linearly proportional to the dark current as it originates from the randomness of the amount of electrons moving from one end of the electrode to the other. On the other hand, the thermal noise ($i_{thermal}$) can be assessed by considering the total parallel resistance (R_p), which only consists of the shunt resistance (R_{shunt}) for a photoconductor-type detector:

$$i_{noise} = \sqrt{\langle i_{shot}^2 \rangle + \langle i_{thermal}^2 \rangle} = \sqrt{2eI_{dark}\Delta f + \frac{4kT}{R_{shunt}}\Delta f}$$

At a 10 V bias, the thermal noise component can be neglected, so only the white shot noise component contributes to the noise current to an appreciable extent.[61,62]

External quantum efficiency (EQE) measurements were performed on the photoconductor-type detectors with different electrode distances at a 10 V voltage bias to determine their effectiveness of charge carrier collection at the Au electrodes (**Figure 7**). The EQE spectra expand over the range of 350 to 600 nm, peaking at their respective n = 2 excitonic absorption peak at 549 and 565 nm for $(BA)_2CsPb_2I_7$, and $(BTBT)_2CsPb_2I_7$, respectively. Here, the *EQE* intensity increases with decreasing electrode distance, which agrees with the delivered photocurrents gathered from the *I-V* measurements. Remarkably, the *EQE* values of the $(BTBT)_2CsPb_2I_7$-based detector are almost doubled with respect to the $(BA)_2CsPb_2I_7$-based one, again likely attributed to the larger crystallites and therefore reduced grain boundaries within the $(BTBT)_2CsPb_2I_7$ thin film. The EQE spectra of 3 different devices are shown in **Figure S11**.

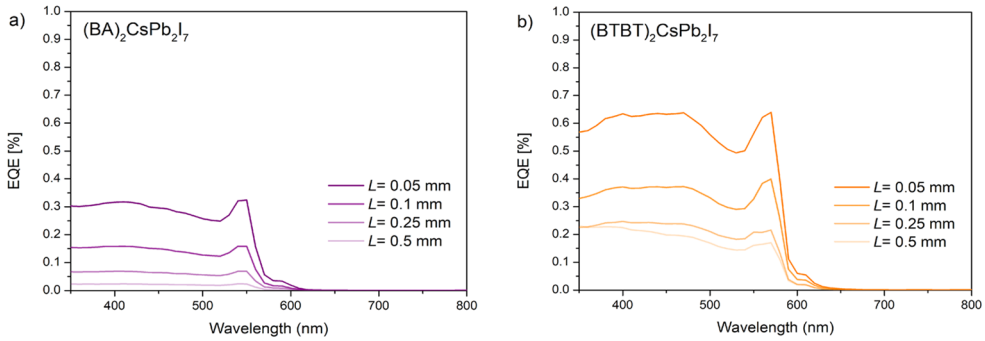

Figure 7. EQE spectra of the $(BA)_2CsPb_2I_7$ (a), and $(BTBT)_2CsPb_2I_7$ (b) detectors with different electrode distances L= 0.05, 0.10, 0.25, and 0.50 mm, under a voltage bias of 10 V.

The specific detectivity D^* was determined for each quasi-2D hybrid perovskite detector with the smallest electrode distance L= 0.05 mm and a respective device area A of 0.026 cm^2 (**Figure 8**).

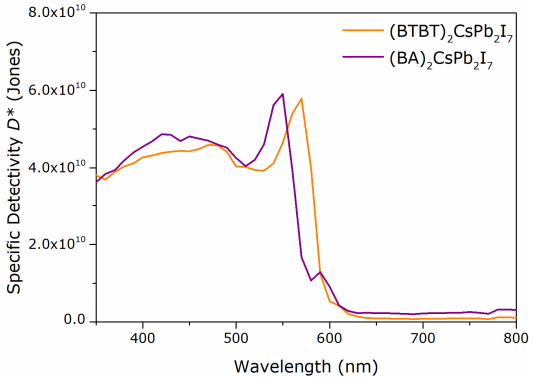

Figure 8. Specific detectivity D^* of a $(BA)_2CsPb_2I_7$ and $(BTBT)_2CsPb_2I_7$ photoconductor-type detector as a function of wavelength, with electrode distance L= 0.05 mm. To assess device reproducibility, three detectors were prepared for each perovskite film (supporting **Figure S12**), the average value of the 3 curves of the 3 devices is shown here.

Our $(BTBT)_2CsPb_2I_7$-based detectors show similar a specific detectivity D^* compared to the state-of-the-art BA-based detectors. Although the photocurrent and EQE are higher for the BTBT-based detectors, the dark current is slightly higher for these detectors compared to the BA-based ones, resulting in similar values for the specific detectivity.

2.5 Conclusions

In conclusion, we demonstrated the potential of using a tailored polyheterocyclic aromatic benzothieno[3,2-*b*]benzothiophene (BTBT) cation in efficiently stabilizing the cesium lead(II) iodide black phase through dimension engineering of a quasi-2D hybrid perovskite $(BTBT)_2CsPb_2I_7$. *In-situ* temperature-controlled XRD showed the vastly superior thermal stability of the $(BTBT)_2CsPb_2I_7$ thin film compared to the state-of-the-art butylammonium (BA)-based $(BA)_2CsPb_2I_7$ thin film. Moreover, the moisture stability of the thin films was monitored by XRD and UV-vis spectroscopy. Here, the $(BTBT)_2CsPb_2I_7$ thin film displayed excellent phase stability for 152 days when exposed to 77% RH at room temperature in the dark, whereas the $(BA)_2CsPb_2I_7$ thin film showed significant degradation already after a single day. Therefore, we have clearly illustrated the benefit of inserting a more rigid, hydrophobic polyheterocyclic aromatic cation instead of a flexible aliphatic one, in greatly enhancing the structural integrity of the quasi-2D hybrid perovskite and inhibiting degradation towards the undesirable, photoinactive yellow δ-phase or lead(II) iodide.

By performing TRMC measurements, a slightly higher local microwave photoconductivity in the $(BTBT)_2CsPb_2I_7$ thin film was measured compared to the $(BA)_2CsPb_2I_7$ thin film, yielding slightly longer charge carrier diffusion lengths. Photoconductor-type detectors based on $(BTBT)_2CsPb_2I_7$ demonstrated a significant increase in photocurrent and external quantum efficiency and a similar specific detectivity as compared to the BA-based detectors. Future research will focus on clarifying the relationship between the rigidity of the large organic ammonium cation and the intrinsic and device stability of the quasi-2D hybrid perovskite.

3. Experimental section

3.1 Chemicals and reagents

Lead iodide (PbI_2, 99.999%) was obtained from Lumtec and cesium iodide (99.999% trace metals basis) was purchased at Merck. Hydroiodic acid (HI, 57% w/w aq., distilled, unstabilized), sodium hydrosulfide hydrate ($NaSH.xH_2O$), 3-chloropropanoyl chloride, aluminum trichloride ($AlCl_3$), methyl sulfoxide (DMSO, 99.7%, extra dry), *N*,*N*-dimethylacetamide (DMAC, 99.5%, extra dry) and lithium aluminum hydride ($LiAlH_4$) were purchased from Acros Organics and used as received. 2-Chlorobenzaldehyde (99%) was

purchased from Fisher Scientific. Sodium diformylamide (>97%) and butyl ammonium iodide (BAI, 97%) were purchased from TCI. For purification, BAI was dissolved in MeOH (4 mL) and poured into Et_2O (200 mL). The resulting precipitate was dried under vacuum to afford BAI as a white product before use. HCl (37%) was purchased from VWR. All solvents and reagents were used as received. The dry DMF that was used to make the precursor solutions, dichloromethane (DCM), toluene, and diethyl ether (Et_2O) were obtained from a solvent purification system (MBRAUN SPS-800). All other solvents (reagent grade) were purchased from Fisher Scientific.

3.2 Thin-film deposition

All precursor solutions were filtered through a PTFE syringe filter (0.45 μm mash) before use. Quartz substrates were cleaned through successive sonication steps in the following order of solvents (detergent water, deionized water, acetone, and isopropanol; 15 min for each step), followed by a UV-ozone treatment of 15 min. The precursor solutions were deposited as thin films on quartz substrates by spin coating *via* a one-step method and annealed (thermal or solvent vapor annealing) on a hotplate in a glove box under a nitrogen atmosphere (< 0.1 ppm O_2, < 0.1 ppm H_2O). Afterward, the samples were stored in a glovebox and only removed for analysis.
$(BA)_2CsPb_2I_7$: Stoichiometric amounts of butylamine hydroiodide (BAI), cesium iodide (CsI), and PbI_2 were dissolved in dry DMF:DMAC 8:2 (0.3 M) under continuous stirring at 65 °C for 30 min. The thin films were thermally annealed at 130 °C for 10 min. Spin-coating: 2000 rpm, 2000 rpm/s, 20 s.
$(BTBT)_2CsPb_2I_7$: Stoichiometric amounts of the BTBT iodide salt, cesium iodide (CsI), and PbI_2 were dissolved in dry DMF:DMSO 9:1 (0.3 M) under continuous stirring at 65 °C for 30 min. The thin films were solvent vapor annealed at 210 °C for 5 min. In this method, a 15 μL droplet of dry DMSO was put on the inner wall of a petri dish. When the thin film is covered by the petri dish on the hot plate, the droplet evaporates and generates a DMSO-containing atmosphere for the film during thermal annealing. Afterward, the crystalline thin film was removed from the hot plate. Spin-coating: 2000 rpm, 2000 rpm/s, 20 s.
The same processing conditions were applied for the films used for the *in-situ* measurements.

3.3 Characterization

The samples for the moisture stability measurements were stored in a desiccator with a saturated NaCl solution. The RH was measured using a humidity sensor.
Optical absorption spectra were measured on a Cary 5000 UV-Vis-NIR spectrophotometer from Agilent Technologies; a cleaned quartz substrate was used as a calibration background.
Photoluminescence (PL) experiments were performed at room temperature under excitation with a 405 nm pulsed diode laser (Thorlabs, NPL41C, 6 ns pulse length and 4.1 nJ per pulse). Backscattered PL emission was diffracted in a grating spectrograph (Andor, Kymera 328i-D2-SIL) and registered by a linear CCD detector (Andor, iDus 416-LDC-DD). Unwanted laser reflections were eliminated from the spectrum by means of a 474 nm long-wavelength pass color filter in front of the spectrograph entrance. In order to avoid photo-degradation, the devices were mounted in N_2 atmosphere in an airtight sample holder. All spectra were corrected for the spectral response of the set-up determined using a calibrated light source (Avantes, AvaLight-HAL-CAL-Mini).
X-ray diffraction measurements on thin films were performed at room temperature in ambient atmosphere on a Bruker D8 Discover diffractometer with a parallel beam geometry using a Göbel mirror and CuKα radiation, with an one-dimensional detector (Lynxeye). *In-situ* XRD measurements were carried out on a Bruker D8 Discover XRD system equipped with a Cu X-ray source (λ = 1.5406 Å) and a linear X-ray detector. The samples were put on a sample heating

stage inside a closed annealing chamber. The XRD measurements were carried out under N_2 atmosphere with a continuous nitrogen flow rate of 500 sccm at atmospheric pressure. Samples were heated via a stepwise temperature profile from RT up to 290 °C in steps of 10 °C. The temperature was measured with a K-type thermocouple. Every 10 °C the temperature was stabilized for several seconds before an XRD scan from 2-35° in 2 theta was taken at that specific temperature.

Thermogravimetric analysis was performed on a Q500 analyzer from TA instruments using a Pt sample cup with a temperature profile of 10°C per min under a N_2 flow of 100 mL per min.

Time-resolved microwave conductivity measurements were performed at room temperature with pulsed laser excitation (repetition rate 10 Hz) at 500 nm. The photon intensities were determined using a laser power/energy meter (LabMax-TOP) and the optical densities of the neutral density filters. During the experiment, the thin films (1.5 cm x 2.1 cm) were placed in a sealed microwave cell under dry nitrogen atmosphere to prevent sample degradation. The temporal resolution is limited by the width of the laser pulse (3.5 ns) and the response time of the system (18 ns). The fraction of absorbed light (F_A) at 500 nm was determined from the UV/Vis absorption spectrum.

The thin film thicknesses were determined using a Bruker DektakXT profilometer.

SEM measurements were performed on a Zeiss GeminiSEM 450. The AFM measurements were performed with a JPK NanoWizard 3 AFM (JPK Instruments AG, Berlin, Germany) using AC mode under ambient atmosphere. AppNano Silicon ACTA-50 tips with a cantilever length ~125 mm, spring constant ~40 N m^{-1} and resonance frequency ~300 kHz were utilized. The scan angle, set point height, gain values and scan rate were corrected according to the AFM tip calibration.

Devices were made by spin-coating films of a $(BA)_2MAPb_2I_7$, $(BA)_2CsPb_2I_7$, and $(BTBT)_2CsPb_2I_7$ precursor solution (prepared as described above) on quartz substrates, followed by either thermal annealing or solvent vapor annealing. On top of the resulting film, 80 nm of Au was evaporated through a shadow mask to obtain electrodes with interdigitating finger structures. Next, silver paste was applied to the edges of the substrate to make electrical contact between the evaporated Au electrode and the pins of the measuring cell. The devices were measured from – 15 V till + 15 V in steps of 0.5 V, either in the dark or under 1 sun A.M 1.5G illumination. The *I-V* curves in darkness of all photoconductor-type detectors were evaluated using a Keithley 2400 source meter. EQE measurements were performed using a homebuilt setup with a Newport Apex illuminator (100 W Quartz Tungsten Halogen lamp) as light source and a Newport Cornerstone 130° monochromator. A chopper frequency of 135 Hz was applied on the monochromated light and the photocurrent measured using a Stanford SR830 lock-in amplifier. The signal was pre-amplified using a DLPCA-200 amplifier from FEMTO, under 10 V (amplification 10^6, full bandwidth, DC mode).

4. Acknowledgements
P.-H.D. is a special research fund (BOF) doctoral (Ph.D.) student at UHasselt/IMO. M.M. and A.M. are SB Ph. D. fellows at FWO (No. 1S20118N and No. 1115721N respectively). W.T.M.V.G., M.V.L., L.L., K.V. and D.V. acknowledge the FWO for the funding of the SBO project PROCEED (FWOS002019N) and the senior FWO research project G043320N. S.M. is a BOF (Ph.D.) student at UHasselt/IMO (grant nr. BOF19OWB15). S.G. acknowledges the Research Foundation – Flanders (FWO Vlaanderen) for funding his Ph.D. fellowship. C.D. and D.D. acknowledge FWO-Vlaanderen and the Special Research Fund BOF of Ghent University (GOA project, Grant No. 01G01019) for funding. Z.W. and F.G. acknowledge the project "Chirality-induced spin selectivity in electron transport" (project nr. 680.92.18.01) of the research programme "Natuurkunde Vrije Programmas", which is (partly) financed by the Dutch Research Council (NWO) and of which this publication is a part. The work has been carried out in the context of the Solliance network (www.solliance.eu), from which UHasselt is a member. Additionally, UHasselt is a partner in the Energyville Consortium (http://www.energyville.be/about-energyville).

Supporting Information

Supporting Information is available from the Wiley Online Library or from the author.

Received: ((will be filled in by the editorial staff))
Revised: ((will be filled in by the editorial staff))
Published online: ((will be filled in by the editorial staff))

References

[1] M. K. Assadi, S. Bakhoda, R. Saidur, H. Hanaei, *Renew. Sustain. Energy Rev.* **2018**, *81*, 2812.

[2] C. R. Dong, Y. Wang, K. Zhang, H. Zeng, *EnergyChem* **2020**, *2*, 100026.

[3] NREL, *NREL. Efficiency chart.*, **2022**.

[4] R. L. Milot, R. J. Sutton, G. E. Eperon, A. A. Haghighirad, J. Martinez Hardigree, L. Miranda, H. J. Snaith, M. B. Johnston, L. M. Herz, *Nano Lett.* **2016**, *16*, 7001.

[5] B. Conings, J. Drijkoningen, N. Gauquelin, A. Babayigit, J. D'Haen, L. D'Olieslaeger, A. Ethirajan, J. Verbeeck, J. Manca, E. Mosconi, F. De Angelis, H.-G. Boyen, *Adv. Energy Mater.* **2015**, *5*, 1500477.

[6] T. A. Berhe, W.-N. Su, C.-H. Chen, C.-J. Pan, J.-H. Cheng, H.-M. Chen, M.-C. Tsai, L.-Y. Chen, A. A. Dubale, B.-J. Hwang, *Energy Environ. Sci.* **2016**, *9*, 323.

[7] L. Gu, D. Zhang, M. Kam, Q. Zhang, S. Poddar, Y. Fu, X. Mo, Z. Fan, *Nanoscale* **2018**, *10*, 15164.

[8] D. Thrithamarassery Gangadharan, D. Ma, *Energy Environ. Sci.* **2019**, *12*, 2860.

[9] G. E. Eperon, S. D. Stranks, C. Menelaou, M. B. Johnston, L. M. Herz, H. J. Snaith, *Energy Environ. Sci.* **2014**, *7*, 982.

[10] D. Wang, M. Wright, N. K. Elumalai, A. Uddin, *Sol. Energy Mater. Sol. Cells* **2016**, *147*, 255.

[11] R. J. Sutton, G. E. Eperon, L. Miranda, E. S. Parrott, B. A. Kamino, J. B. Patel, M. T. Hörantner, M. B. Johnston, A. A. Haghighirad, D. T. Moore, H. J. Snaith, *Adv. Energy Mater.* **2016**, *6*, 1502458.

[12] G. E. Eperon, G. M. Paternò, R. J. Sutton, A. Zampetti, A. A. Haghighirad, F. Cacialli, H. J. Snaith, *J. Mater. Chem. A* **2015**, *3*, 19688.

[13] R. E. Beal, D. J. Slotcavage, T. Leijtens, A. R. Bowring, R. A. Belisle, W. H. Nguyen, G. F. Burkhard, E. T. Hoke, M. D. McGehee, *J. Phys. Chem. Lett.* **2016**, *7*, 746.

[14] F. Bella, P. Renzi, C. Cavallo, C. Gerbaldi, *Chem. - A Eur. J.* **2018**, *24*, 12183.

[15] T. Zhang, M. I. Dar, G. Li, F. Xu, N. Guo, M. Grätzel, Y. Zhao, *Sci. Adv.* **2017**, *3*, e1700841.

[16] A. Marronnier, G. Roma, S. Boyer-Richard, L. Pedesseau, J.-M. Jancu, Y. Bonnassieux, C. Katan, C. C. Stoumpos, M. G. Kanatzidis, J. Even, *ACS Nano* **2018**, *12*, 3477.

[17] Y. Wang, Y. Chen, T. Zhang, X. Wang, Y. Zhao, *Adv. Mater.* **2020**, *32*, 2001025.

[18] C. C. Stoumpos, C. D. Malliakas, J. A. Peters, Z. Liu, M. Sebastian, J. Im, T. C. Chasapis, A. C. Wibowo, D. Y. Chung, A. J. Freeman, B. W. Wessels, M. G. Kanatzidis, *Cryst. Growth Des.* **2013**, *13*, 2722.

[19] J. B. Hoffman, A. L. Schleper, P. V. Kamat, *J. Am. Chem. Soc.* **2016**, *138*, 8603.

[20] P. Luo, W. Xia, S. Zhou, L. Sun, J. Cheng, C. Xu, Y. Lu, *J. Phys. Chem. Lett.* **2016**, *7*, 3603.

[21] R. F. Kahwagi, S. T. Thornton, B. Smith, G. I. Koleilat, *Front. Optoelectron.* **2020**, *13*, 196.

[22] R. Herckens, W. T. M. Van Gompel, W. Song, M. C. Gélvez-Rueda, A. Maufort, B. Ruttens, J. D'Haen, F. C. Grozema, T. Aernouts, L. Lutsen, D. Vanderzande, *J. Mater. Chem. A* **2018**, *6*, 22899.

[23] W. T. M. Van Gompel, R. Herckens, M. Mertens, P. Denis, B. Ruttens, J. D'Haen, K. Van Hecke, L. Lutsen, D. Vanderzande, *ChemNanoMat* **2021**, *7*, 1013.

[24] P.-H. Denis, M. Mertens, W. T. M. Van Gompel, K. Van Hecke, B. Ruttens, J. D'Haen, L. Lutsen, D. Vanderzande, *Chem. Mater.* **2021**, *33*, 5177.

[25] C. C. Stoumpos, D. H. Cao, D. J. Clark, J. Young, J. M. Rondinelli, J. I. Jang, J. T. Hupp, M. G. Kanatzidis, *Chem. Mater.* **2016**, *28*, 2852.

[26] D. H. Cao, C. C. Stoumpos, O. K. Farha, J. T. Hupp, M. G. Kanatzidis, *J. Am. Chem. Soc.* **2015**, *137*, 7843.

[27] J.-F. Liao, H.-S. Rao, B.-X. Chen, D.-B. Kuang, C.-Y. Su, *J. Mater. Chem. A* **2017**, *5*, 2066.

[28] Y. Jiang, J. Yuan, Y. Ni, J. Yang, Y. Wang, T. Jiu, M. Yuan, J. Chen, *Joule* **2018**, *2*, 1356.

[29] C. C. Stoumpos, C. M. M. Soe, H. Tsai, W. Nie, J.-C. Blancon, D. H. Cao, F. Liu, B. Traoré, C. Katan, J. Even, A. D. Mohite, M. G. Kanatzidis, *Chem* **2017**, *2*, 427.

[30] M. Zhou, C. Fei, J. S. Sarmiento, H. Wang, *Sol. RRL* **2019**, *3*, 1800359.

[31] A. H. Proppe, R. Quintero-Bermudez, H. Tan, O. Voznyy, S. O. Kelley, E. H. Sargent, *J. Am. Chem. Soc.* **2018**, *140*, 2890.

[32] J. Liu, J. Leng, K. Wu, J. Zhang, S. Jin, *J. Am. Chem. Soc.* **2017**, *139*, 1432.

[33] A. Hadi, B. J. Ryan, R. D. Nelson, K. Santra, F. Lin, E. W. Cochran, M. G. Panthani, *Chem. Mater.* **2019**, *31*, 4990.

[34] W. T. M. Van Gompel, R. Herckens, K. Van Hecke, B. Ruttens, J. D'Haen, L. Lutsen, D. Vanderzande, *Chem. Commun.* **2019**, *55*, 2481.

[35] M. D. Smith, B. A. Connor, H. I. Karunadasa, *Chem. Rev.* **2019**, *119*, 3104.

[36] K. Jemli, P. Audebert, L. Galmiche, G. Trippé-Allard, D. Garrot, J.-S. Lauret, E. Deleporte, *ACS Appl. Mater. Interfaces* **2015**, *7*, 21763.

[37] X. Li, J. Yang, Z. Song, R. Chen, L. Ma, H. Li, J. Jia, J. Meng, X. Li, M. Yi, X. Sun, *ACS Appl. Energy Mater.* **2018**, *1*, 4467.

[38] C. Ortiz-Cervantes, P. I. Román-Román, J. Vazquez-Chavez, M. Hernández-Rodríguez, D. Solis-Ibarra, *Angew. Chemie Int. Ed.* **2018**, *57*, 13882.

[39] J. V. Passarelli, D. J. Fairfield, N. A. Sather, M. P. Hendricks, H. Sai, C. L. Stern, S. I. Stupp, *J. Am. Chem. Soc.* **2018**, *140*, 7313.

[40] M. C. Gélvez-Rueda, W. T. M. Van Gompel, R. Herckens, L. Lutsen, D. Vanderzande, F. C. Grozema, *J. Phys. Chem. Lett.* **2020**, *11*, 824.

[41] N. Marchal, W. Van Gompel, M. C. Gélvez-Rueda, K. Vandewal, K. Van Hecke, H.-G. Boyen, B. Conings, R. Herckens, S. Maheshwari, L. Lutsen, C. Quarti, F. C. Grozema, D. Vanderzande, D. Beljonne, *Chem. Mater.* **2019**, *31*, 6880.

[42] M. Van Landeghem, W. Van Gompel, R. Herckens, L. Lutsen, D. Vanderzande, S. Van Doorslaer, E. Goovaerts, *J. Phys. Chem. C* **2021**, *125*, 18317.

[43] W. T. M. Van Gompel, R. Herckens, P.-H. Denis, M. Mertens, M. C. Gélvez-Rueda, K. Van Hecke, B. Ruttens, J. D'Haen, F. C. Grozema, L. Lutsen, D. Vanderzande, *J. Mater. Chem. C* **2020**, *8*, 7181.

[44] K. Du, Q. Tu, X. Zhang, Q. Han, J. Liu, S. Zauscher, D. B. Mitzi, *Inorg. Chem.* **2017**,

56, 9291.

[45] M. Yuan, L. N. Quan, R. Comin, G. Walters, R. Sabatini, O. Voznyy, S. Hoogland, Y. Zhao, E. M. Beauregard, P. Kanjanaboos, Z. Lu, D. H. Kim, E. H. Sargent, *Nat. Nanotechnol.* **2016**, *11*, 872.

[46] J. Zhou, Y. Chu, J. Huang, *ACS Appl. Mater. Interfaces* **2016**, *8*, 25660.

[47] A. Vassilakopoulou, D. Papadatos, I. Zakouras, I. Koutselas, *J. Alloys Compd.* **2017**, *692*, 589.

[48] W. Peng, J. Yin, K.-T. Ho, O. Ouellette, M. De Bastiani, B. Murali, O. El Tall, C. Shen, X. Miao, J. Pan, E. Alarousu, J.-H. He, B. S. Ooi, O. F. Mohammed, E. Sargent, O. M. Bakr, *Nano Lett.* **2017**, *17*, 4759.

[49] Z.-H. Zheng, H.-B. Lan, Z.-H. Su, H.-X. Peng, J.-T. Luo, G.-X. Liang, P. Fan, *Sci. Rep.* **2019**, *9*, 17422.

[50] Z. Song, S. C. Watthage, A. B. Phillips, B. L. Tompkins, R. J. Ellingson, M. J. Heben, *Chem. Mater.* **2015**, *27*, 4612.

[51] Y. Fu, M. T. Rea, J. Chen, D. J. Morrow, M. P. Hautzinger, Y. Zhao, D. Pan, L. H. Manger, J. C. Wright, R. H. Goldsmith, S. Jin, *Chem. Mater.* **2017**, *29*, 8385.

[52] E. Amerling, S. Baniya, E. Lafalce, C. Zhang, Z. V. Vardeny, L. Whittaker-Brooks, *J. Phys. Chem. Lett.* **2017**, *8*, 4557.

[53] W. T. M. Van Gompel, R. Herckens, K. Van Hecke, B. Ruttens, J. D'Haen, L. Lutsen, D. Vanderzande, *ChemNanoMat* **2019**, *5*, 323.

[54] H. Zheng, G. Liu, L. Zhu, J. Ye, X. Zhang, A. Alsaedi, T. Hayat, X. Pan, S. Dai, *Adv. Energy Mater.* **2018**, *8*, 1800051.

[55] T. J. Savenije, A. J. Ferguson, N. Kopidakis, G. Rumbles, *J. Phys. Chem. C* **2013**, *117*, 24085.

[56] M. C. Gélvez-Rueda, M. B. Fridriksson, R. K. Dubey, W. F. Jager, W. van der Stam, F. C. Grozema, *Nat. Commun.* **2020**, *11*, 1901.

[57] O. G. Reid, M. Yang, N. Kopidakis, K. Zhu, G. Rumbles, *ACS Energy Lett.* **2016**, *1*, 561.

[58] T. J. Savenije, D. Guo, V. M. Caselli, E. M. Hutter, *Adv. Energy Mater.* **2020**, *10*, 1903788.

[59] R. H. Kingston, In *Encyclopedia of Physical Science and Technology*, Elsevier, **2003**, pp. 237–253.

[60] Z. Liu, D. Liu, H. Chen, L. Ji, H. Zheng, Y. Gu, F. Wang, Z. Chen, S. Li, *Nanoscale Res. Lett.* **2019**, *14*, 304.

[61] Y. Fang, A. Armin, P. Meredith, J. Huang, *Nat. Photonics* **2019**, *13*, 1.

[62] S. Gielen, C. Kaiser, F. Verstraeten, J. Kublitski, J. Benduhn, D. Spoltore, P. Verstappen, W. Maes, P. Meredith, A. Armin, K. Vandewal, *Adv. Mater.* **2020**, *32*, 2003818.

[63] S. M. Sze, K. K. Ng, *Physics of Semiconductor Devices*, 3rd Editio., Wiley, New York, **2006**.

[64] V. Venugopalan, R. Sorrentino, P. Topolovsek, D. Nava, S. Neutzner, G. Ferrari, A. Petrozza, M. Caironi, *Chem* **2019**, *5*, 868.

Table of contents entry:

We stabilize the photoactive black phase of cesium lead(II) iodide by the formation of a quasi-2D perovskite containing a benzothieno[3,2-b]benzothiophene (BTBT) large organic ammonium cation. The thermal stability and the moisture stability are significantly enhanced compared to a butylammonium (BA) quasi-2D perovskite. Photoconductor-type detectors based on $(BTBT)_2CsPb_2I_7$ demonstrate an increased external quantum efficiency compared to the BA-based reference detectors.

*Paul-Henry Denis, Martijn Mertens, Wouter T.M. Van Gompel, Arthur Maufort, Bart Ruttens, Zimu Wei, Melissa Van Landeghem, Sigurd Mertens, Sam Gielen, Davy Deduytsche, Christophe Detarvernier, Laurence Lutsen, Ferdinand Grozema, Koen Vandewal, Dirk Vanderzande**

Quasi-2D hybrid perovskite formation using benzothieno[3,2-b]benzothiophene (BTBT) ammonium cations: substantial cesium lead(II) iodide black phase stabilization

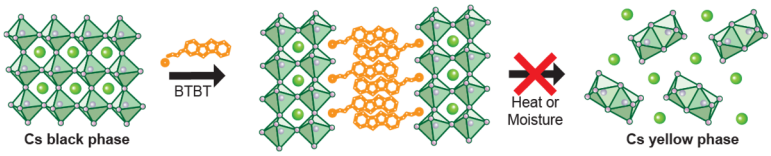

Supporting Information

Quasi-2D hybrid perovskite formation using benzothieno[3,2-*b*]benzothiophene (BTBT) ammonium cations: substantial cesium lead(II) iodide black phase stabilization

*Paul-Henry Denis, Martijn Mertens, Wouter T.M. Van Gompel, Arthur Maufort, Bart Ruttens, Zimu Wei, Melissa Van Landeghem, Sigurd Mertens, Sam Gielen, Davy Deduytsche, Christophe Detarvernier, Laurence Lutsen, Ferdinand Grozema, Koen Vandewal, Dirk Vanderzande**

Synthesis of 2-(3-propylamine)benzothieno[3,2-b]benzothiophene, hydroiodide (BTBT)

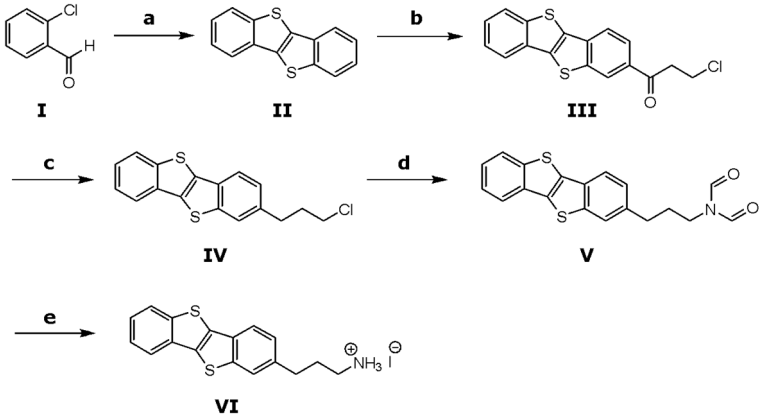

Figure S1. Synthetic pathway to obtain BTBT: a) $NaSH.xH_2O$, NMP, 80 °C → 180 °C, overnight; b) 3-chloropropanoyl chloride, $AlCl_3$, DCM, -78 °C → RT, 4 h; c) $LiAlH_4$, $AlCl_3$, Et_2O, DCM, RT, overnight; d) Sodium diformylamide, DMF, 80 °C, 22 h; e) HCl, EtOH, 110 °C, 18 h; then HI, $CHCl_3$, RT, 5 h.

Benzothieno[3,2-*b*]benzothiophene (**II**): A solution of 2-chlorobenzaldehyde (**I**) (16.03 mL, 142.3 mmol) in NMP (40 mL) was heated to 80 °C and stirred for 1 h. Subsequently, sodium hydrosulfide hydrate (23.81 g, 284.6 mmol) was added to the reaction mixture, then heated to 180 °C and stirred for 16 h. Afterwards, the reaction mixture was poured into a saturated NH_4Cl solution (200 mL) at 0 °C. The precipitate was filtered off and washed with water and acetone. The crude product was purified by recrystallization from toluene to obtain **I** as an off-white solid (22.00 g, 66%). ^{1}H NMR (400 MHz, Chloroform-*d*) δ 7.93 (ddd, *J* = 7.9, 1.3, 0.7 Hz, 2H), 7.89 (ddd, *J* = 7.9, 1.4, 0.7 Hz, 2H), 7.49 – 7.44 (m, 2H), 7.41 (ddd, *J* = 8.0, 7.2, 1.4 Hz, 2H).

2-Benzothieno[3,2-*b*]benzothiophene-3-chloro-1-propanone (**III**): **II** (3.653 g, 15.20 mmol) was dissolved in dry DCM (500 mL) under a N_2 atmosphere and cooled to -10 °C. Then, $AlCl_3$ (2.027 g, 15.20 mmol) was added and the reaction mixture was cooled to -78 °C. Next, 3-chloropropanoyl chloride (1.45 mL, 15.20 mmol) was added drop-wise and the mixture was stirred for 4 h. The reaction was then quenched with ice water and diluted with MeOH, causing the precipitation of the product. The product was filtered off, washed with water (2 x 50 mL) and MeOH (2 x 50 mL) and dried under vacuum. The residue was purified by flash chromatography (PE:$CHCl_3$ 80:20) to obtain **III** as an off-white solid (3.87 g, 77%). ^{1}H NMR (400 MHz, Chloroform-*d*) δ 8.56 (dd, *J* = 1.5, 0.7 Hz, 1H), 8.06 (dd, *J* = 8.4, 1.6 Hz, 1H), 7.99 – 7.90 (m, 3H), 7.56 – 7.43 (m, 2H), 3.99 (t, *J* = 6.8 Hz, 2H), 3.58 (t, *J* = 6.8 Hz, 2H).

2-(3-Chloropropyl)-benzothieno[3,2-*b*]benzothiophene (**IV**): Aluminum trichloride (3.900 g, 29.25 mmol) was suspended in dry Et_2O (100 mL) under a N_2 atmosphere and a suspension of $LiAlH_4$ (1.110 g, 29.25 mmol) in dry DCM (25 mL) was added drop-wise. **III** (3.870 g, 11.70 mmol) in dry DCM (400 mL) was added drop-wise and the reaction was stirred overnight at ambient temperature. Afterwards, the reaction mixture was cooled to 0 °C and quenched by adding a solution of 2 M HCl until pH = 2 was obtained. The mixture was extracted with $CHCl_3$ (3 x 100 mL). Then, the organic layer was dried with magnesium sulfate, filtered and the solvent was evaporated under reduced pressure. The residue was purified by flash chromatography (PE:$CHCl_3$ 10:1), to obtain **IV** as an off-white solid (2.23 g, 60%). ^{1}H NMR (400 MHz, Chloroform-*d*) δ 7.92 (dt, *J* = 7.9, 0.9 Hz, 1H), 7.88 (ddd, *J* = 7.9, 1.4, 0.7 Hz, 1H), 7.81 (dd, *J* = 8.1, 0.6 Hz, 1H), 7.75 (dd, *J* = 1.5, 0.7 Hz, 1H), 7.50 – 7.43 (m, 1H), 7.42 – 7.36 (m, 1H), 7.30 (dd, *J* = 8.1, 1.5 Hz, 1H), 3.58 (t, *J* = 6.4 Hz, 2H), 2.95 (t, *J* = 7.4 Hz, 2H), 2.26 – 2.12 (m, 2H).

2-(3-Diformylamidepropyl)-benzothieno[3,2-*b*]benzothiophene (**V**): **IV** (1.365 g, 4.31 mmol) was dissolved in dry DMF (40 mL) and subsequently sodium diformylamide (0.792 g, 8.33 mmol) was added. Under N_2 atmosphere, the mixture was stirred at 80 °C for 22 h. The reaction mixture was then quenched with aqueous NH_4Cl (0.5 M) and extracted with $CHCl_3$. The organic fractions were combined and washed with aqueous NH_4Cl, water, and brine. After drying with magnesium sulphate and filtering, the solvent was evaporated under reduced pressure. Subsequent column chromatography with gradient elution from hexanes/EtOAc 2:1 -> 0:1 yielded **V** as a yellow solid (0.944 g, 62%). ^{1}H NMR (400 MHz, Chloroform-*d*) δ 8.84 (s, 2H), 7.91 (ddd, J = 7.9, 1.1, 0.7 Hz, 1H), 7.87 (ddd, J = 7.9, 1.4, 0.7 Hz, 1H), 7.80 (dd, J = 8.1, 0.6 Hz, 1H), 7.73 (dd, J = 1.5, 0.7 Hz, 1H), 7.48 – 7.43 (m, 1H), 7.42 – 7.36 (m, 1H), 7.29 (dd, J = 8.1, 1.6 Hz, 1H), 3.75 (t, J = 7.5 Hz, 2H), 2.85 – 2.75 (m, 2H), 2.08 – 1.93 (m, 2H).

2-(3-propylamine)benzothieno[3,2-*b*]benzothiophene, hydroiodide (**VI**): **V** (0.944 g, 2.67 mmol) was suspended in EtOH, after which HCl (37 wt% in water, 877 µL, 10.7 mmol) was added. The mixture was heated to 110°C under N_2 atmosphere. After about 30 min, the suspension had turned into a clear solution. A new precipitate was formed overnight and the reaction mixture was cooled to room temperature after 18 h. 250 mL of an alkaline buffer was added (0.5 M $NaHCO_3$ + 0.25 M KOH, pH = 11), followed by extraction with $CHCl_3$. The organic fractions were combined, dried with magnesium sulphate, and concentrated under reduced pressure until about 250 mL was left. HI (57 wt% in water, unstabilized) was extracted three times with a 1:10 (v/v) tributyl phosphate/$CHCl_3$ mixture to remove impurities. Immediately after this extraction, 388 µL (2.94 mmol) was transferred to the BTBT solution in $CHCl_3$. The resulting mixture was left to react at ambient temperature under Ar atmosphere for 5 h, during which a precipitate was formed. Subsequent vacuum filtration, washing with Et_2O, and drying under high vacuum yielded **VI** as a faint yellow solid (0.964 g, 85%). ^{1}H NMR (400 MHz, DMSO-d_6) δ 8.15 (dd, J = 7.4, 1.3 Hz, 1H), 8.05 – 8.01 (m, 1H), 8.01 (s, 1H), 7.99 (d, J = 6.0 Hz, 1H), 7.66 (s, 3H), 7.57 – 7.49 (m, 1H), 7.51 – 7.45 (m, 1H), 7.43 – 7.37 (m, 1H), 2.84 (dt, J = 7.7 Hz, 4H), 1.99 – 1.88 (m, 2H). ^{13}C NMR (400 MHz, DMSO-d_6) δ 141.93, 141.40, 138.69, 132.70, 132.39, 132.23, 130.63, 126.17, 125.39 (integrates for 2 carbon atoms), 124.50, 123.74, 121.65, 121.55, 38.40, 31.81, 28.83.

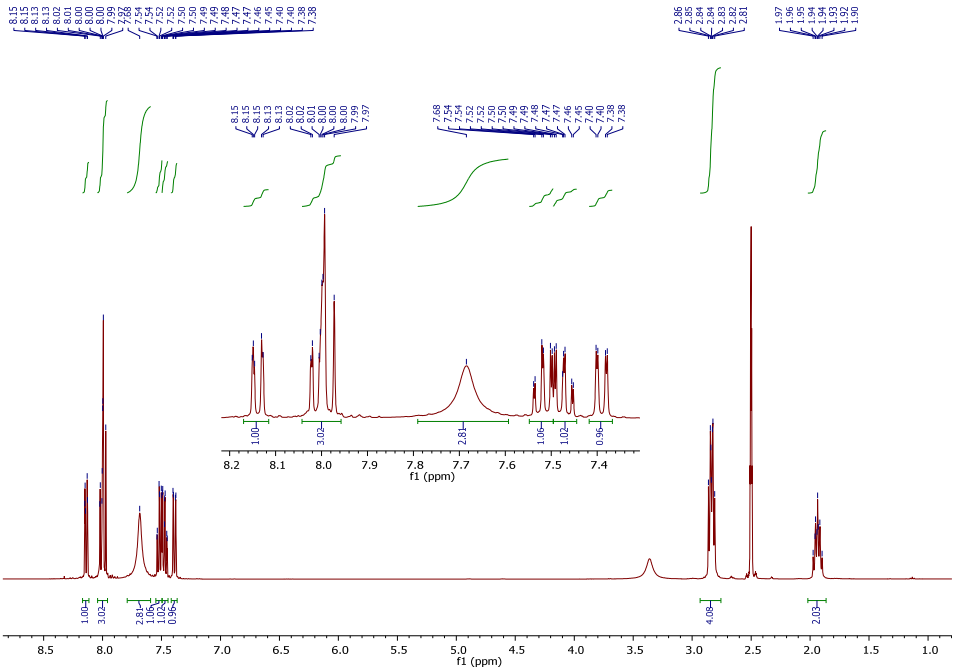

Figure S2.[1]H NMR spectrum of 2-(3-propylamine)benzothieno[3,2-b]benzothiophene, hydroiodide (VI) in DMSO-d_6. The signal at 2.5 ppm originates from residual DMSO solvent; the signal at 3.4 ppm corresponds to residual water.

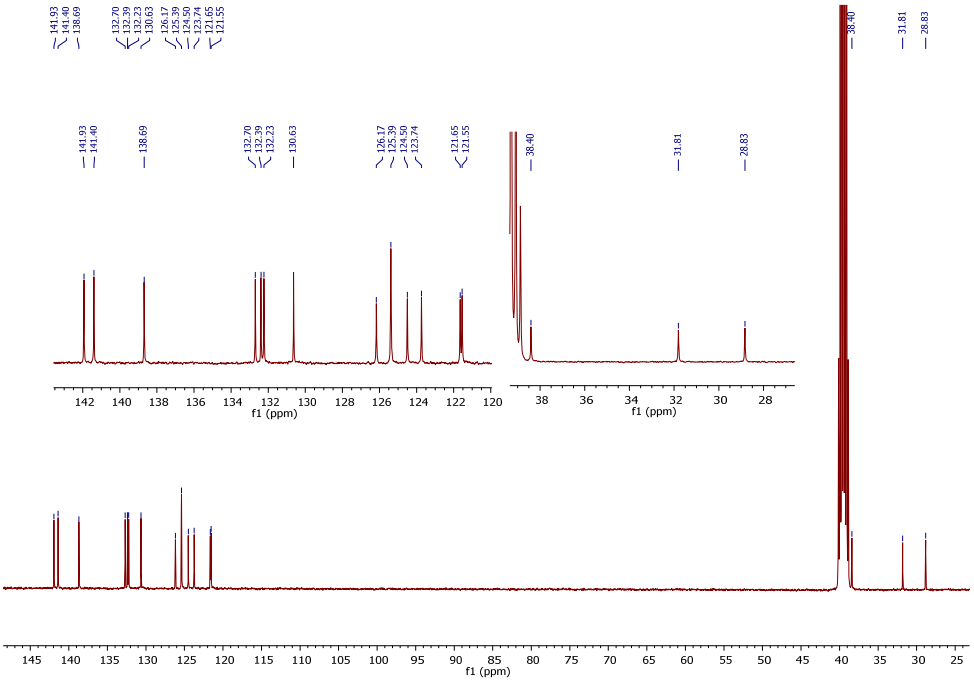

Figure S3. [13]C NMR spectrum of 2-(3-propylamine)benzothieno[3,2-b]benzothiophene, hydroiodide (VI) in DMSO-*d*6. The signal at 39.5 ppm corresponds to DMSO.

Optical and structural properties of a $(BTBT)_2PbI_4$ n = 1 thin film

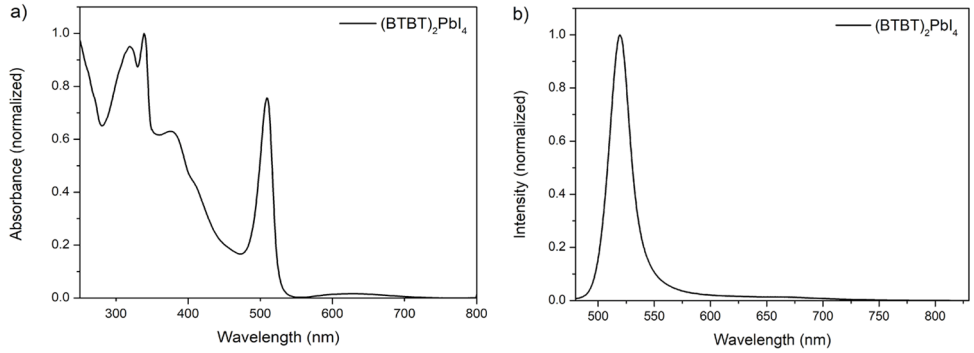

Figure S4. Absorption and emission spectra of a spin-coated $(BTBT)_2PbI_4$ thin film using solvent annealing (SA) at 150 °C for 15 min. The emission spectrum was obtained by exciting the samples at 430 nm.

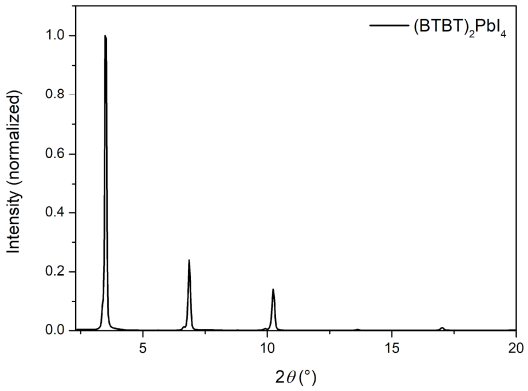

Figure S5. X-ray diffraction patterns of a spin-coated $(BTBT)_2PbI_4$ thin film using solvent annealing (SA) at 150 °C for 15 min.

Thin film morphology and roughness

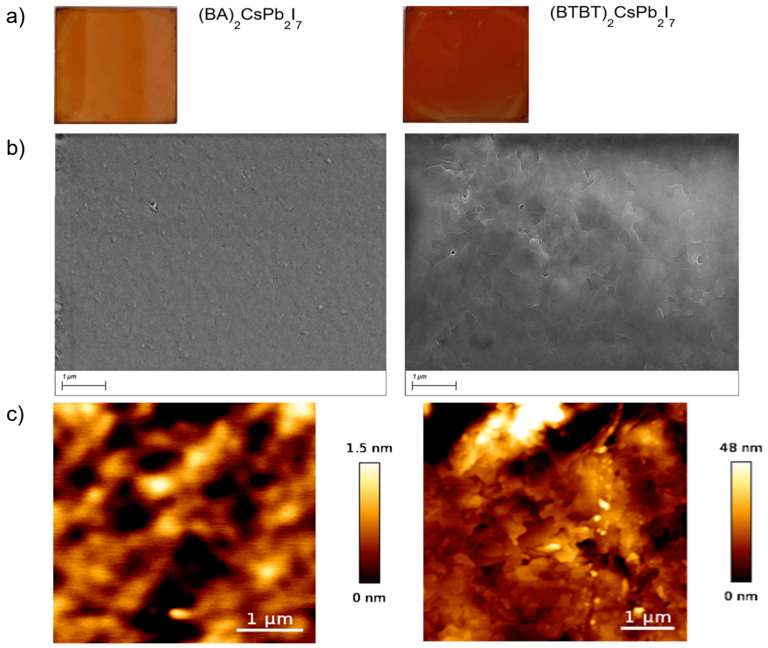

Figure S6. Photographs (a), SEM micrographs (b), and AFM images (c) of a spin-coated $(BA)_2CsPb_2I_7$, and $(BTBT)_2CsPb_2I_7$ thin film. SEM images obtained using a Everhart-Thornley detector = 5 kV.

Normalized in-situ X-ray diffraction patterns (thermal stability)

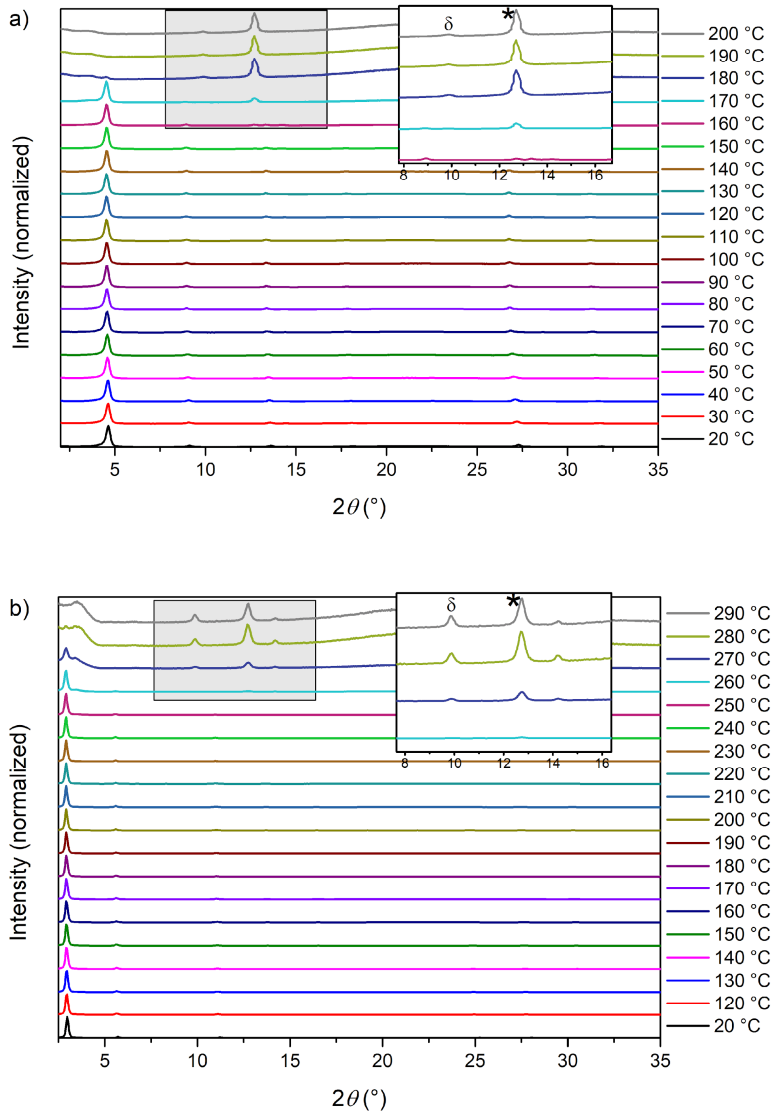

Figure S7. *In-situ* x-ray diffraction patterns (normalized) as a function of temperature starting from the spin-coated thin films of $(BA)_2CsPb_2I_7$ (a), and $(BTBT)_2CsPb_2I_7$ (b) before the *in-situ* experiment. The weak reflections of the degradation product PbI_2 (*) and the yellow δ-phase (δ) are magnified (inset) in the relevant temperature range.

Thermogravimetric analysis of organic ammonium cations

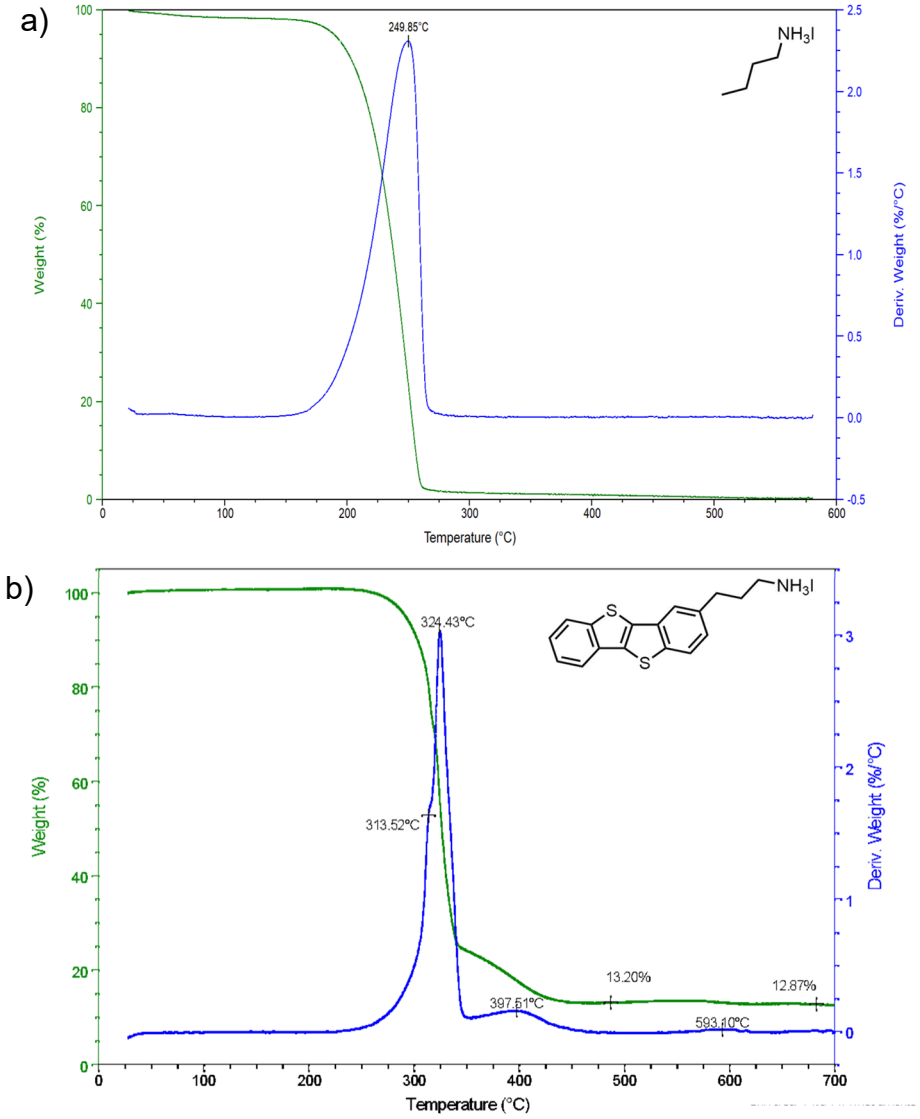

Figure S8. Thermal gravimetric analysis (TGA) curve of the butyl ammonium BA cation (a) and BTBT cation (b) as a function of temperature, at a heating rate 10 °C per min under N_2 atmosphere.

Absolute In-situ X-ray diffraction patterns (moisture stability)

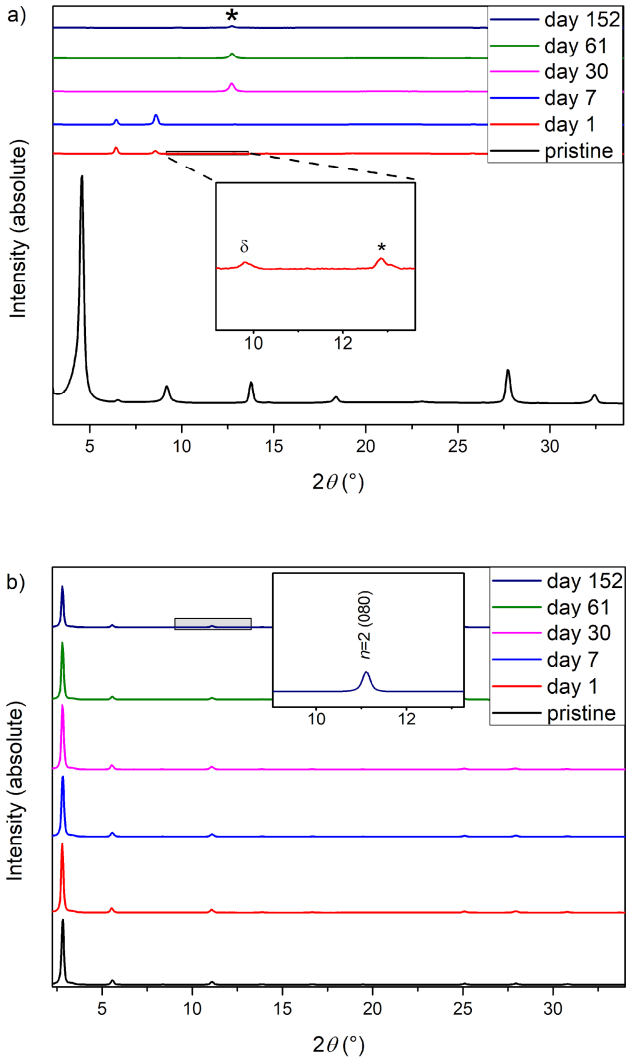

Figure S9. X-ray diffraction patterns (absolute) of a spin-coated $(BA)_2CsPb_2I_7$ thin film annealed at 130 °C for 10 min (a), and a $(BTBT)_2CsPb_2I_7$ thin film annealed at 210 °C for 5 min (b), being stored at 77% RH and measured at different times over the course of 152 days. For $(BA)_2CsPb_2I_7$, the weak reflections of the degradation product PbI_2 (*) and yellow δ-phase (δ) are apparent after one day. For $(BTBT)_2CsPb_2I_7$, no degradation occurs after 152 days.

Light to dark current ratio of the photoconductor-type detectors

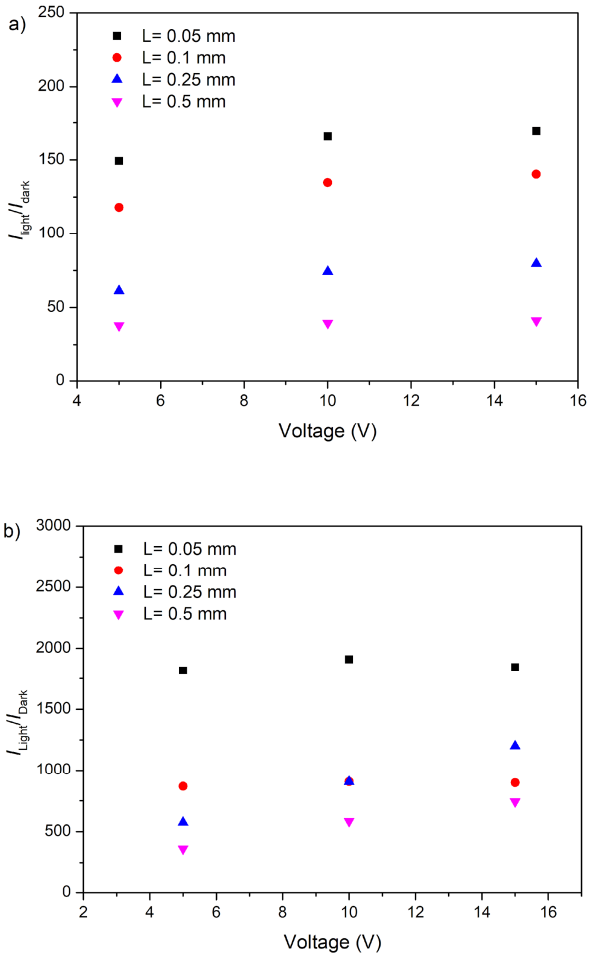

Figure S10. I_{light}/I_{dark} ratio in function of voltage bias (V) of the respective $(BA)_2CsPb_2I_7$ (a), and $(BTBT)_2CsPb_2I_7$ (b) photoconductor-type detectors with varying electrode distances.

Photoconductor-type detector performances

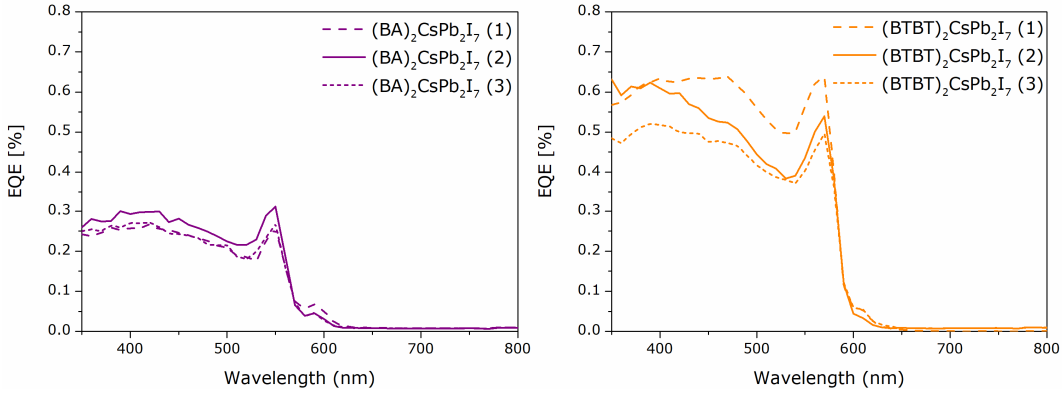

Figure S11. External quantum efficiency (EQE) spectra of the respective $(BA)_2CsPb_2I_7$, and $(BTBT)_2CsPb_2I_7$ photoconductor-type detectors, with electrode distance L= 0.05 mm.

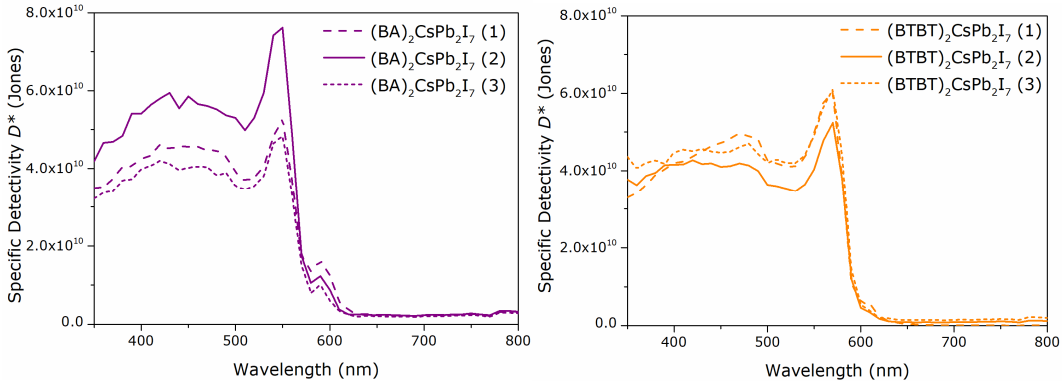

Figure S12. Specific detectivity curves of the respective $(BA)_2CsPb_2I_7$, and $(BTBT)_2CsPb_2I_7$ photoconductor-type detectors as a function of wavelength, with electrode distance L= 0.05 mm.